1   Trace-element heterogeneity in rutile linked to dislocation structures: Implications for Zr-in-rutile

2   geothermometry

3   Dislocations as fast-diffusion pathways

4   Rick Verberne[1, 2*], Hugo W. van Schrojenstein Lantman[3**], Steven. M. Reddy[1, 2], Matteo Alvaro[3],

5   David Wallis[5], Denis Fougerouse[1, 2], Antonio Langone[4], David W. Saxey[1], William D.A. Rickard[1]

6   [1]Geoscience Atom Probe Facility, John de Laeter Centre, Curtin University, Perth, WA 6845,

7   Australia.

8   [2]School of Earth and Planetary Sciences, Curtin University, Perth, WA 6845, Australia

9   [3]Department of Earth and Environmental Sciences, University of Pavia, Via A. Ferrata, 1 I-27100

10   Pavia, Italy

11   [4]Institute of Geosciences and Earth Resources, National Research Council (C.N.R), 27100 Pavia, Italy

12   [5]Department of Earth Sciences, University of Cambridge, Cambridge CB2 3EQ, United Kingdom

13   *Current address: Center for Star and Planet Formation, Globe Institute, University of Copenhagen,

14   Øster Voldgade 5–7, DK-1350 Copenhagen

15   **Current address: Department of Geosciences, The Njord Centre, University of Oslo, Oslo, Norway

16   **ABSTRACT**

17   The trace-element composition of rutile is commonly used to constrain *P-T-t*-conditions for a wide

18   range of metamorphic systems. However, recent studies have demonstrated the redistribution of

19   trace elements in rutile via high-diffusivity pathways and dislocation-impurity associations related to

20   the formation and evolution of microstructures. Here we investigate trace-element migration in low-

21   angle boundaries formed by dislocation creep in rutile within an omphacite vein of the Lago di

22   Cignana unit (Western Alps, Italy). Zr-in-rutile thermometry and inclusions of quartz in rutile and of

23   coesite in omphacite constrain the conditions of rutile deformation to around the prograde

24   boundary from high pressure to ultra-high pressure (~2.7 GPa) at temperatures of 500–565 °C. These

25   results constrain the conditions of deformation of rutile and its effects on composition. Crystal-

26   plastic deformation of a large rutile grain results in low-angle boundaries that generate a total

27   misorientation of ~25°. Dislocations constituting one of these low-angle boundaries are enriched in

28   common and uncommon trace elements, including Fe and Ca, providing evidence for diffusion and

29   trapping of trace elements along the dislocation cores. The role of dislocation microstructures as

30   fast-diffusion pathways must be evaluated when applying high-resolution analytical procedures as

31   compositional disturbances might lead to erroneous interpretations for Ca and Fe. In contrast, our

32   results indicate a trapping mechanism for Zr.

33

34   **Keywords:** Rutile, Low-Angle Boundaries, Plastic deformation, Diffusion, Trace elements

35   **1. INTRODUCTION**

36   Rutile is a common accessory mineral formed at mid- to lower-crustal metamorphic

37   conditions (Dachille, Simons, & Roy, 1968) and is stable in ultra-high temperature (UHT) and

38   pressure (UHP) environments (Jamieson & Olinger, 1969; Mei, Wang, Shang, & Liu, 2014; Withers,

39   Essene, & Zhang, 2003). The trace-element and isotopic compositions of rutile are routinely analysed

40   to constrain the timing and conditions of geological events. Two of the most important applications

41 of rutile compositional data are U-Pb geochronology (Mezger, Hanson, & Bohlen, 1989; T. Zack, von

42 Eynatten, & Kronz, 2004) and Zr-in-rutile thermometry (Kohn, 2020; T. Zack, Moraes, & Kronz, 2004).

43 These applications are a significant addition to the traditional options for geothermobarometry and

44 geochronology in the often-restrictive mineral assemblages of UHP metamorphic rocks (Cutts &

45 Smit, 2018; DesOrmeau, Gordon, Little, Bowring, & Chatterjee, 2017; Gao, Zheng, Xia, & Chen, 2014;

46 T Zack & Luvizottow, 2006). Furthermore, rutile has the capacity to retain information about the *P-T-*

47 *t*-path by preserving mineral and fluid inclusions (Hart, Storey, Bruand, Schertl, & Alexander, 2016;

48 Hart, Storey, Harley, & Fowler, 2018; Ni et al., 2008).

49 The use of rutile is underpinned by the assumptions that element mobility during geological

50 events subsequent to initial equilibration is well understood and inclusions remain shielded from

51 chemical interaction with the exterior of the host grain. However, many studies have reported

52 disturbances in trace-element distribution and isotopic compositions (Kohn, 2020; Kooijman,

53 Mezger, & Berndt, 2010; Smye & Stockli, 2014; Zhou et al., 2020). These effects have generally been

54 attributed to trace-element migration via volume diffusion. More recently, the presence of twin

55 boundaries, low-angle boundaries (LABs, i.e., subgrain boundaries), and high-angle grain boundaries

56 have been proposed to affect the distribution and mobility of trace elements in natural rutile (Moore

57 et al., 2020; Zack & Kooijman, 2017). Volume diffusion in larger rutile grains is ineffective at

58 temperatures below approximately 600 °C for Pb and 650 °C for Zr (Cherniak, 2000; Cherniak,

59 Manchester, & Watson, 2007). However, grain boundaries form fast pathways for intergranular

60 diffusion (Klinger & Rabkin, 1999), particularly in the presence of a fluid.

61 Rates of intragranular diffusion can be enhanced beyond those of volume diffusion through

62 the presence of intragranular microstructures that contribute to dislocation-impurity pair migration

63 (Imai & Sumino, 1983; Petukhov & Klyuchnik, 2012) and high-diffusivity pathways (Love, 1964;

64 Sutton, Balluffi, & Sutton, 1995). Trace-element migration by dislocation-impurity associations relies

65 on the coupled migration of dislocations and trace elements trapped in and around them. This

66 mechanism can lead to removal of trace elements into the grain-boundary network (Imai & Sumino,

67   1983; Petukhov & Klyuchnik, 2012). Alternatively, the increasing concentration of solutes can

68   immobilise the migrating dislocation leading to a localised trace-element enrichment (Cottrell &

69   Bilby, 1949; Dubosq, Rogowitz, Schweinar, Gault, & Schneider, 2019; Imai & Sumino, 1983; Petukhov

70   & Klyuchnik, 2012). High-diffusivity pathways can form along microstructures related to growth and

71   deformation, such as dislocations, low- and high-angle boundaries, or twin boundaries (Fougerouse,

72   Reddy, et al., 2021; Keller, Abart, Wirth, Schmid, & Kunze, 2006; Love, 1964; Plümper et al., 2012;

73   Reddy, Timms, Pantleon, & Trimby, 2007; Timms, Kinny, & Reddy, 2006; Vukmanovic et al., 2014;

74   Lund, Piazolo, & Harley 2006; Verberne et al., 2022).

75   Identifying these effects in geological materials has remained challenging due to limitations

76   in the spatial resolutions of techniques capable of measuring chemical and isotopic composition

77   (Reddy et al., 2006; Timms et al., 2006; Timms et al., 2011). Advances in analytical techniques allow

78   for correlation among high-spatial resolution chemical and isotopic data with micro- and nanoscale

79   structures. Atom probe tomography (APT) is one such technique with high spatial resolution

80   providing chemical and isotopic information in three dimensions (Gault, Moody, Cairney, & Ringer,

81   2012; Larson, Prosa, Ulfig, Geiser, & Kelly, 2013). Over the last five years, this technique has proven

82   to be a powerful tool within the field of Earth sciences (Reddy et al., 2020; Saxey, Moser, Piazolo,

83   Reddy, & Valley, 2018). The combination of APT with analytical techniques employing larger spot

84   sizes (e.g., LA-ICP-MS or SIMS) allows for correlation of geochronological data (Peterman et al., 2019;

85   Peterman et al., 2016; Seydoux-Guillaume et al., 2019; Valley et al., 2014; Valley et al., 2015;

86   Verberne et al., 2020). Furthermore, APT can reveal a structure-chemistry relationship down to the

87   nanoscale when applied in combination with high-resolution structural imaging techniques, such as

88   electron backscatter diffraction (EBSD), transmission Kikuchi diffraction (TKD), or transmission

89   electron microscopy (TEM) (Fougerouse, Reddy, et al., 2021; Fougerouse et al., 2019; Fougerouse et

90   al., 2018; Kirkland, Fougerouse, Reddy, Hollis, & Saxey, 2018; Montalvo et al., 2019; Piazolo et al.,

91   2016; Reddy et al., 2020; Reddy et al., 2016; Verberne et al., 2022).

92   This contribution investigates the characteristics and underlying processes of trace-element

93   heterogeneities associated with dislocation structures in low-angle boundaries related to crystal-

94   plastic deformation of rutile. The rutile is located within deformed omphacite veins from the UHP-

95   low-temperature (LT) metamorphic Lago di Cignana unit (LCU), Italy. The LCU provides an excellent

96   opportunity for studying the effect of diffusion along dislocations. The minerals were strained during

97   HP deformation resulting in dislocation microstructures whilst the low temperatures ensured that

98   volume diffusion was ineffective and thus did not obscure the effect of dislocations. By the

99   combination of a range of analytical techniques, the study first constrains the growth and

100   deformation history of rutile in relation to *P-T* conditions. Then, micro- and nanoscale analytical

101   techniques are applied to investigate the relation between plastic deformation of rutile and

102   segregation of trace elements. The results highlight the complexity that can arise from the interplay

103   between different structural features, and how these structures correlate with nanoscale chemical

104   heterogeneities.

105   **2.   GEOLOGICAL SETTING**

106   **2.1   Geological overview**

107   The Lago di Cignana unit is a lens of UHP metabasic and metasedimentary rocks within the

108   Zermatt-Saas unit (ZSU), an ophiolitic unit of generally high-pressure (HP) metamorphic grade (Fig.

109   1). The ZSU was subducted and underwent eclogite-facies metamorphism during the Alpine orogeny

110   (Rubatto, Gebauer, & Fanning, 1998), reaching peak metamorphic conditions of 600–630 °C, 2.7–2.9

111   GPa determined for metasediments (Reinecke, 1998) and 590–605 °C, >3.2 GPa based on eclogites

112   (Groppo, Beltrando, & Compagnoni, 2009). Subsequently, the LCU was exhumed and juxtaposed

113   with the overlying lower-grade (greenschist-amphibolite facies) Combin zone (Fig. 1) (Amato,

114   Johnson, Baumgartner & Beard, 1999; Kirst & Leiss, 2017; Reddy et al., 2003). As one of few exposed

115   ophiolitic units exhumed after Alpine UHP metamorphism, the LCU is a key locality for insight into

116   fluid-rock interaction at great depth in subduction zones (Frezzotti, Selverstone, Sharp, &

117 Compagnoni, 2011; Halama, Konrad-Schmolke & De Hoog, 2020; Van Schrojenstein Lantman,

118 Scambelluri, Gilio, Wallis & Alvaro, 2021).

119   The LCU has been the subject of numerous geochronological studies aimed at pinpointing

120 the timing of formation and subduction of the Piemonte-Ligurian oceanic crust. Prograde to peak

121 metamorphic ages have been previously determined as 48.8 ± 2.1 Ma (Lu-Hf garnet-omphacite-

122 whole rock, Lapen et al., 2003), 44.1 ± 0.7 Ma (U/Pb zircon mean age, Rubatto et al., 1998), and 40.6

123 ± 2.6 Ma (Sm-Nd garnet-whole rock, Amato et al., 1999). Early exhumation of the LCU or ZSU as a

124 whole is dated as 41.6 ± 0.2 and 39.8 ± 0.2 Ma (Rb-Sr phengite-clinozoisite, Skora et al., 2015), 41—

125 39 Ma (K-Ar white mica range of ages, Gouzu et al., 2016), 38 ± 2 Ma (Rb-Sr phengite-whole rock,

126 Amato et al., 1999) and 45–36 (Rb-Sr various minerals, range of ages, Reddy et al., 1999). Rb-Sr

127 white-mica ages of 39–36 Ma for the Combin Fault represent the exhumation leading to

128 emplacement of the ZSU below the Combin Zone, in agreement with rapid exhumation after peak

129 metamorphism (Kirst & Leiss, 2017; Reddy et al., 2003; Reddy, Wheeler, & Cliff, 1999).

130 **2.2   LCU eclogite**

131   The main lithologies of the LCU are quartzite and schist locally bearing garnetite lenses, calc-

132 schist, marble, and eclogite (Forster et al., 2004). Garnet- and glaucophane-rich zones in the eclogite

133 may reflect compositional differences due to fluid-rock interaction (Van Schrojenstein Lantman et

134 al., 2021) or related to pillow basalts (Van der Klauw, Reinecke, & Stöckhert, 1997). The peak

135 metamorphic assemblage consists of garnet, omphacite, glaucophane, lawsonite, phengite, rutile,

136 and minor coesite and zircon. The latter two minerals are also present as inclusions in omphacite

137 and garnet (Groppo et al., 2009; King, Bebout, Kobayashi, Nakamura, & Van Der Klauw, 2004).

138 Lawsonite has broken down to pseudomorphs of epidote and paragonite. Titanite, ilmenite, Ca-

139 amphibole, and biotite preserved as inclusions in garnet cores represent an early prograde

140 metamorphic mineral assemblage. The eclogite is rich in TiO_2 (>2 wt. %), resulting in an abundance

141 of rutile (Groppo et al., 2009). A multitude of veins has been identified in the LCU eclogites, mainly

142   consisting of omphacite, glaucophane, quartz (potentially after coesite), epidote/clinozoisite, and

143   retrogressed lawsonite (Borghini et al., unpublished data). The relative timings of vein formation

144   range from UHP metamorphism to retrograde metamorphic stages during exhumation.

145   The deformation of the LCU eclogites has been established in detail. Müller & Compagnoni

146   (2009) indicate that pyroxene pervasively deformed by dislocation creep with dynamic

147   recrystallization resulting from grain-boundary migration. At the onset of extension, the deformation

148   became localized, leading to the formation of shear bands (Van der Klauw et al., 1997). Little to no

149   deformation took place in the eclogites during the first 40 km of exhumation, down to *P-T* conditions

150   of <1.5 GPa, 500–550 °C (Van der Klauw et al., 1997). Following this part of the exhumation, further

151   deformation within eclogites was associated with a retrograde mineral assemblage of hornblende,

152   albite, and epidote (Kirst & Leiss, 2017).

153

154   **3. METHODS**

155   This contribution is a collaboration between the Geoscience Atom Probe group of Curtin

156   University, and the University of Pavia, where measurements were performed concurrently. To

157   ensure that the data obtained represent equivalent material, two near-identical thick sections of 100

158   μm thickness were prepared from the same chip of the hand specimen (Fig. 2b). Work conducted at

159   the University of Pavia focused on multiple grains of a variety of minerals with data acquisition at

160   scales of 1–50 μm, while the complementary work at Curtin University focused on the micro- and

161   nanoscale characterisation of a single large rutile crystal (Grain ID - Rt-1, Fig. 2b,3a). The multiple

162   rutile grains studied at the University of Pavia and those analysed at Curtin University come from the

163   omphacite vein (see sample description).

164 **3.1   Raman Spectroscopy**

165 Raman spectroscopy for the purpose of the identification of mineral inclusions was conducted at the

166 University of Pavia using a Horiba LabRam HR Evolution spectrometer with a holographic grating of

167 1800 grooves/mm. The Horiba is equipped with an Olympus BX41 confocal microscope and operated

168 at a constant temperature of 20 ± 1 °C. Raman spectra were excited using the 514.532 nm line of a

169 solid-state (YAG) laser. The laser power on the sample surface was approximately 1–2 mW. The

170 spectrometer was calibrated by matching the Raman spectrum to the silicon peak at 520.5 cm^{-1}.

171 **3.2   LA-ICP-MS and Zr-in-rutile geothermometry**

172 The trace-element composition of rutile was determined by laser ablation inductively coupled

173 plasma mass spectrometry (LA-ICP-MS) at the Istituto di Geoscienze e Georisorse of the National

174 Research Council in Pavia. The instrument couples an Excimer Laser 193 nm ArF (GeoLas200

175 Microlas) with a Triple Quadrupole (8900 QQQ from Agilent). Elements that were measured are: ^{7}Li,

176 ^{9}Be, ^{11}B, ^{23}Na, ^{25}Mg, ^{27}Al, ^{29}Si, ^{39}K, ^{43}Ca, ^{44}Ca, ^{45}Sc, ^{47}Ti, ^{51}V, ^{53}Cr, ^{55}Mn, ^{57}Fe, ^{59}Co, ^{60}Ni, ^{63}Cu, ^{66}Zn, ^{75}As,

177 ^{85}Rb, ^{88}Sr, ^{89}Y, ^{90}Zr, ^{93}Nb, ^{95}Mo, ^{118}Sn, ^{121}Sb, ^{133}Cs, ^{138}Ba, ^{139}La, ^{140}Ce, ^{141}Pr, ^{146}Nd, ^{149}Sm, ^{151}Eu, ^{157}Gd,

178 ^{159}Tb, ^{163}Dy, ^{165}Ho, ^{167}Er, ^{169}Tm, ^{173}Yb, ^{175}Lu, ^{177}Hf, ^{181}Ta, ^{182}W, ^{208}Pb, ^{232}Th, and ^{238}U. NIST-SRM610 was

179 used as an external standard, whereas Ti was adopted as an internal standard for rutile. In each

180 analytical run, the USGS reference samples BCR2 and NIST612 (Norman, Pearson, Sharma, & Griffin,

181 1996; Pearce et al., 1997; Rocholl et al., 1997) were analysed together with the unknowns for quality

182 control. Precision and accuracy are better than 5% and 10%, respectively. Data reduction was

183 performed using the Glitter software package (Van Actherbergh, 2001). A laser beam, 50 μm in

184 diameter, was employed to analyse 16 spots over six rutile grains, measuring core and rim

185 separately when grain size allowed, and using an average TiO_2 content of 99 wt. % as an internal

186 standard.

187 The concentration of Zr in rutile grown in equilibrium with zircon and quartz/coesite provides

188 temperature estimates that accurately reflect crystallisation temperature (Zack et al., 2004b).

189 Accurate results from Zr-in-rutile geothermometry require constraints on the activities of Zr (aZr)

190 and Si (aSi) (Kohn, 2020; Tomkins, Powell, & Ellis, 2007; Watson, Wark, & Thomas, 2006; Zack,

191 Moraes, et al., 2004). In cases where aSi and/or aZr < 1, the Zr-in-rutile geothermometer will provide

192 over- or underestimates of the temperature, respectively. It is assumed that aSi = aZr = 1 if Zr- and

193 Si-bearing phases (e.g., zircon and quartz) were in equilibrium with rutile (T. Zack, Moraes, et al.,

194 2004). Zr-in-rutile thermometry was applied using the P-sensitive "combined" calibration by Kohn

195 (2020).

196 **3.3 Scanning Electron Microscopy**

197 Rutile was characterised by using the TESCAN MIRA3 field-emission scanning electron microscope at

198 the John de Laeter Centre (JdLC), Curtin University, Perth, Australia. BSE images were collected at a

199 working distance of 15 mm and an accelerating voltage of 20 kV. For combined electron backscatter

200 diffraction (EBSD) and energy dispersive X-ray spectroscopy (EDS) imaging the SEM was operated at

201 a working distance of 15 mm with the stage tilted to 70° andan accelerating voltage of 20 kV was

202 applied. EBSD data were acquired at a step size of 1 μm and the match units for rutile (Swope,

203 Smyth, & Larson, 1995) and omphacite (Oberti & Caporuscio, 1991) were obtained from the

204 American Mineralogist crystallography database (801 448-45x).

205 Transmission Kikuchi Diffraction (TKD) was performed on the APT specimens to assist with

206 targeting the LABs during sample preparation for APT and to provide correlation with APT data. TKD

207 was performed with a step size of 15 nm and at a working distance of 9 mm, 90° tilt, an accelerating

208 voltage of 30 kV.

209 Post-processing of EBSD and TKD data was performed in Matlab®, version R2020b, using the

210 free toolbox MTEX Version 5.3 (Bachmann, Hielscher, & Schaeben, 2010). Images were plotted using

the 'roma' scientific color map of Crameri (2018). Post-processing involved a noise-reduction

procedure by removal of groups of <5 adjacent pixels ('Wild' spikes/shards) with crystal orientations

within 10° of those of their neighbours. The procedure was followed by applying a 5x5 pixel median

filter. The filter smooths the orientations in the EBSD data whilst preserving subgrain boundaries

(see supplementary data DR-1).

3.4   Focussed-Ion-Beam SEM

Specimen preparation for TEM and APT was conducted on the Tescan Lyra Ga^+ Focused Ion

Beam Scanning Electron Microscope (FIB-SEM) (Fig. 3), within the JdLC. The FIB-SEM was operated at

an accelerating voltage of 30 kV. TEM and APT specimens were extracted from one low-angle

boundary in a single grain. The TEM foil was mounted on a copper half-grid and thinned to < 100 nm

followed by a 2 kV cleaning routine to remove damage induced by 30 kV specimen preparation. APT

specimens were precisely targeted using electron-beam deposited markers and followed by the

standard lift-out and sharpening procedures and 2 kV clean-up routine (Rickard et al., 2020). TKD

imaging ensured that the LAB was present close to the apex of the tip after final sample preparation

and consequently within the field-of-view for APT analysis. Final secondary-electron (SE) imaging

was performed in SEM-mode only at a working distance of 6 mm and an accelerating voltage of 10

kV.

3.5   Transmission Electron Microscopy

TEM analysis was performed on the FEI Talos FS200X Field Emission Gun TEM equipped with

a Super-X EDS detector housed in the JdLC, Curtin University, Australia. The TEM was operated at

200 kV. TEM imaging was conducted in both bright- and dark-field (BF and DF) modes. The TEM

diffraction investigation was conducted with the assistance of Kikuchi patterns that were generated

by convergent beam electron diffraction (CBED). A small spot was used to minimize the beam-

related damage to the sample, and the sample was tilted to align a zone axis or meet a two-beam

condition to acquire selected-area diffraction (SAD) patterns. Both BF and DF TEM imaging were

undertaken with the objective apertures after tilting the sample to a diffraction condition within 20°.

Chemical analysis was conducted using the attached two pairs of Super-X detectors. The

TEM is fitted with four scanning transmission electron microscopy (STEM) detection systems: high-

angle annular dark-field (HAADF), upper dark-field (DF4), lower dark-field (DF2), and bright-field (BF).

The contrast in HAADF images results predominantly from chemical/phase differences and the

contrast in BF images results predominantly from orientation differences. The DF4 and DF2

detectors reveal both chemical and orientation contrasts at different angles. TEM, STEM, and EDS

data acquisition were conducted with the Velox software.

3.6   Atom probe tomography

APT analyses were performed on a Cameca Local Electrode Atom Probe (LEAP) 4000X HR at

the Geoscience Atom Probe Facility, Curtin University. The LEAP was operated in laser-assisted mode

at a pulse rate of 200 kHz, a laser pulse energy of 50 pJ, a base temperature of 50 K and a detection

rate of 0.8% (1600 ions s^{-1}) based on recommendations by Verberne et al. (2019). Five needle-

shaped specimens were run in the atom probe yielding 38×10^6–95×10^6 ion counts. All specimens

remained intact after the run. Post-processing was performed using Cameca's Integrated

Visualization and Analysis Software (IVAS) 3.8.0., using a field of 26 V/nm following

recommendations in Denis Fougerouse, Saxey, Rickard, Reddy, & Verberne, 2021. Peaks in the mass

spectra were labelled per individual element for specific ionization states and ranged with a constant

width of 0.2 Da unless clearly resulting in the measurement of background signals. Detailed

information about acquisition and post-processing is provided in supplementary data - DR-2 based

on Blum et al. (2018). For visualization and compositional analyses, isoconcentration surfaces were

computed in 3D using IVAS, with error bars on the proximity histograms given as 1σ (Hellman,

Vandenbroucke, Rusing, Isheim, & Seidman, 2000). Whereas 1D concentration profiles provide

insight into the distribution of elements across individual features, proximity histograms (Hellman et

260   al., 2000) are ideal to visualise the overall extent of trace-element enrichment for a selected feature,

261   as well as providing better statistical insights due to measuring significantly larger volumes.

262   Proximity histograms are measured orthogonal to each point on an isoconcentration surface. The

263   distance is based on the smallest radius of all included features (5 nm). Proximity histograms are

264   based on a 0.8 at. % Fe isoconcentration surface.

265   **4. RESULTS**

266   **4.1   Sample characterization**

267   The studied sample, obtained at grid reference 45°52'42.5"N 7°35'33.3"E (Fig. 1), is an

268   eclogite cross-cut by a network of omphacite veins up to approximately 1 cm in width (Fig. 2a-c). In

269   the outcrop, the vein network appears undeformed to weakly deformed (Fig. 2a). Besides omphacite

270   as the main component, the veins also contain rutile, apatite, and minor glaucophane (Fig. 2). The

271   host eclogite consists mostly of garnet, omphacite of a smaller grain size than in the vein,

272   glaucophane, and abundant rutile grains. Rutile is commonly concentrated at the contact between

273   the host eclogite and the vein (Fig. 2b, c). Locally, the distinction between vein and wall rock is less

274   clear, potentially due to the presence of wall rock-derived grains, such as garnet and rutile, within

275   the vein (Fig. 2b). Most crystals in the vein are up to 1 mm in length and exhibit a shape preferred

276   orientation (sub-vertical in Fig. 2c). In contrast, glaucophane rarely exceeds a grain size of 100 μm.

277   Rutile within the wall rock occurs as grains smaller than 100 μm, which is significantly smaller than

278   rutile in the veins. No deformation features in the vein are visible in the hand specimen or thick

279   section. Primary fluid inclusions with vapour bubble and calcite daughter crystal, as identified with

280   Raman spectroscopy, are locally present within omphacite in the vein (Fig. 2e). Garnet in the host

281   eclogite exhibits erratic compositional zonation, as visualised by BSE imaging (Fig. 2f).

4.2 Inclusion characterization

Coesite, apatite, and zircon are identified within omphacite by Raman spectroscopy, the latter mineral inclusion being the most abundant (Fig. 4a, b, d). Calcite is also present, although only as daughter crystals in primary fluid inclusions. Zircon, omphacite, and rutile were identified as inclusions in garnet. Inclusions hosted in rutile are difficult to identify due to the strong Raman signal of rutile. Nevertheless, quartz inclusions were identified in rutile (Fig. 4c, e). No radial fractures were observed around these inclusions. Ubiquitous exsolution platelets in rutile (Fig. 4c) could not be identified using Raman spectroscopy.

4.3 Rutile geochemistry

Figure 5a presents the range of concentrations of all elements in the rutile that consistently yielded concentrations above the detection limit. The full dataset is available in supplementary data DR-3, locations of analysed rutile grains are given in supplementary data DR-7. Measured Zr concentrations in rutile are in the range 31.5–52.6 ppm, taking into account the 1σ uncertainty (Fig. 5b). Most rutile cores contain higher Zr concentrations than their respective rims, and overall differences in Zr concentration exist between grains beyond the uncertainty of the measurements. As a result, the Zr-in-rutile thermometry does not result in, and reflect, a single temperature. Using the full range of Zr concentrations including analytical uncertainty, and a pressure range from 2.0 GPa (lower-*P* estimate for the first appearance of rutile, after Groppo et al., 2009) up to the quartz-coesite transition at 2.7–2.8 GPa, Zr-in-rutile thermometry results in a range of 500–565 °C (Fig. 5b). Propagated temperature uncertainties using the applied combined calibration are on the order of 10–15 °C (Kohn, 2020).

4.4 Microstructural analysis

The various substructures within the rutile are characterized by different analytical techniques. The BSE images presented in Figure 3b reveal a LAB evident as subtle orientation contrast and show the

306   presence of Fe-rich exsolution platelets crosscutting the LAB. These thin, Fe-rich platelets are visible

307   throughout the entire grain, both in contact with LABs and isolated from them. The angles are

308   systematic within a grain. Measured at one location, the apparent angles are acute, 35° between

309   two platelets, and intersecting the LAB at apparent angles of 69° and 78° in Figure 3b.

310   The EBSD maps reveal that rutile, present within the omphacite vein, is deformed (Fig. 6a).

311   This deformation is expressed in the form of LABs with misorientation angles of up to approximately

312   2° across individual boundaries (Fig. 6b) resulting in a total misorientation of approximately 25°

313   across the grain (Fig. 6c). The EBSD maps of the whole grain show that the LAB traces change in

314   orientation, with the dominant orientation being subhorizontal (100–280°) and parallel to [100] (Fig

315   6c, d), and with the misorientation axis being <010> at our region of interest (Fig. 6c, d). However,

316   the misorientation axes also have a second preferred orientation centered on <110> (Fig. 6c, d),

317   resulting in crystal directions, such as [100], exhibiting spreads of about ~19° in the longitudinal

318   direction and ~9° in the latitudinal direction. These complex misorientation characteristics indicate

319   the operation of multiple slip systems.

320   TKD maps of the APT specimens revealed that two specimens contain LABs that were originally near

321   perpendicular to the surface of the thin section (Fig. 7). The two specimens come from the same

322   crystal approximately 5 μm apart, yet the boundary observed within the specimens dips in opposite

323   directions. The geometry of these low angle boundaries, and the misorientation and dispersion axes

324   close to being parallel with [110] for M2 and parallel to [010] M5, suggest the active slip system to

325   be {110}[001] (M2) and {010}[001] (M5).

326   **4.5   Nanoscale structure and composition**

327   The TEM foil HAADF and dark-field images indicate that the LAB is composed of

328   approximately parallel dislocations aligned along the boundaries (Fig. 8b–c). The separation of

329   dislocations varies in the range 5–35 nm (Fig. 8c-d). The LABs are not planar, but instead exhibit an

330   irregular pattern and are offset by steps approximately 10 nm in height (Fig. 8b, white arrow).

14

331   As expected from the APT TKD maps, two of the five analysed specimens contained a LAB

332   within the field of view.

333   The 3D reconstructions of M2 (Fig. 9a) and M5 (Fig. 9d) reveal the presence of a mix of

334   chemically distinct linear features that intersect. These are highlighted by contrasting distributions of

335   Fe (red) and Ca (purple) and are visualised using Fe isoconcentration surfaces (0.8 at. % Fe) in Figure

336   9, overlain with the Ca distribution. For a 3D representation of the data see supplementary data DR-

337   4, 5, 6. Note that the 2D images of 3D features sometimes create false angles.

338   APT chemical analysis of the rutile matrix demonstrates a homogeneous distribution of trace

339   elements outside the LAB, with a TiO_2 concentration of approximately 96 at. % and H concentration

340   of 2–3 at. % (1, 2, and 3 Da) (Fig. 10). Pb is only observed above the background as $^{208}Pb^{++}$ (104 Da)

341   and is distributed homogeneously.

342   Chemical heterogeneities are only observed in relation to the LAB in M2 and M5 and not in

343   the rutile matrix. Sub-horizontal, parallel linear features parallel to <100> are present in both

344   specimens. As <100> is also the most common misorientation axis (Fig. 6), these features are

345   interpreted as edge dislocations (Fig. 9). The dislocations within a single specimen all lie in the same

346   plane with spacings of approximately 10 nm. In both specimens, the dislocations are enriched in

347   trace elements (supplementary data DR-6), compensated by reductions in Ti concentration (Fig. 9,

348   10). The differences in H concentration are due to the OH-species, mainly OH+ (17 Da) while H-

349   species at 1, 2 and 3 Da in the mass spectrum remain homogeneous (supplementary data DR-6). The

350   concentrations are evaluated using 1D concentration profiles (Fig. 10). These profiles exhibit Fe

351   concentrations reaching 1 at. % in the LAB. Al, Si, and Ca concentrations are also higher in the LAB

352   than the matrix at <0.05–0.25 at. %, 0.15 at. % and 0.1 at. %, respectively, across individual

353   structures.

354   Approximately every 50 nm, the plane in which the dislocations lie is offset by roughly 10 nm

355   (Fig. 9c). These 'steps' still exhibit the dislocation pattern within their substructure (Fig. 9c). The

356   dislocations have higher concentrations of trace elements compared to the matrix. The chemical

composition of these steps is displayed as a 1D concentration profile (Fig. 10). Similar to the

dislocations outside the steps, those inside the steps are associated with elevated concentrations of

Fe (0.5–4.2 at. %), Al (<0.05–0.45 at. %), and Si (<0.05–0.1 at. %) relative to the concentrations in the

matrix. In addition, Zr concentrations in the dislocations are 0.1 at. %, up from <0.05 at. % in the

matrix and other dislocations outside the steps. The Ca signal in this feature is notably low at <0.05

at. %.

Extending from the dislocations in M5 are two near vertical Fe-enriched features that we will

refer to as platelets (Fig. 9b). The acute angle between these two platelets is 59° (Fig. 9f). The

platelets intersect the LAB at 60° and 61°. The chemistry of these platelets is comparable to the

chemistry of the steps but the degree of enrichment of Fe is less and Ca and Si are absent. Fe

reaches concentrations of 2 at. % (up from 0.5 at. % in the matrix) and H increases from

approximately 2 at. % to 3.5 at. %. The concentration of Zr within the 1D profile is 0.06 at. % and the

concentration of Al is 0.12 at. %.

Two entangled, sub-vertical dislocations are present within M2 and are connected to the

previously described horizontal dislocations (Fig. 9a). Where the two dislocations are separate, they

exhibit different chemical signatures. Branch 1, left in Figure 8f, exhibits concentrations of Fe and Al

of 1.8 at. % and 0.15 at. %, respectively. Branch 2 yields a slightly stronger enrichment in Fe at 2.1 at.

% and higher concentrations of Al at 0.42 at. %. Furthermore, this branch also exhibits

concentrations of 0.23 at. % Ca, 0.19 at. % Si and 0.08 at. % Zr.

Where the two dislocations intersect, the Fe and H concentrations increase further relative

to the individual branches to 4 at. % and 6 at. %, respectively. The Al concentration also increases

slightly compared to the individual branches reaching 0.45 at. %, while Ca, Si, and Zr concentrations

remain at the same levels as in Branch 2 (Fig. 10). To better visualise the difference between the two

branches and the intersection points, a 1D concentration profile, crossing both branches, and

moving along the entire length of the dislocations was recorded (supplementary data DR-3). Note

that all elements reach their maximum concentration in the centre of the isoconcentration surface

383   (Fig 9f), all elements are co-located and do not form a core shell structure as seen for high-angle

384   boundaries (Fougerouse et al., 2019).

385   Proximity histograms can visualise the overall extent of trace-element enrichment (Fig 10f).

386   The TiO_2 concentration is approximately 96 at. % in the matrix and decreases by approximately 5 at.

387   % within the substructures. The Fe concentration increases from approximately 0.1 at. % to 2.3 at. %

388   and the H signal increases from approximately 2.3 at. % to 4.2 at. %, together making up the bulk of

389   trace-element enrichment. Furthermore, V increases from approximately 0.26 at. % to 0.45 at. %, Cr

390   concentrations increase from approximately 0.17 at. % to 0.26 at. %. Al, Ca, Si, and Sn are present in

391   concentrations of <0.025 at. % within the matrix but reach concentrations of 0.42, 0.12, 0.12, and

392   0.07 at. % respectively within the substructures. Zr, important for temperature estimations, is

393   present in concentrations of <0.01 at. % in the matrix but increases to 0.025 at. % within features in

394   the low-angle boundary.

395   **5.   DISCUSSION**

396   **5.1   Relative timing and conditions of geological events**

397   Before assessing the influence of LABs and associated dislocations on rutile geochemistry,

398   the relative timing of growth and deformation, and the *P-T* conditions during both, must be

399   constrained. These constraints also help to assess the potential for volume diffusion, allowing us to

400   distinguish other transport mechanisms. Omphacite within the rutile-bearing vein contains coesite

401   inclusions (Fig. 4b), whereas quartz inclusions are preserved inside the investigated rutile grains (Fig.

402   4c). These inclusions indicate that 1) the vein formed at ultrahigh-pressure metamorphic conditions

403   and 2) rutile growth occurred within the quartz stability field, thus not during the UHP metamorphic

404   peak. The Zr concentrations in rutile (Fig. 5) correspond to temperatures that are either on the high-

405   pressure prograde path, or low-pressure retrograde path. No evidence is observed for significant

406   mineral reactions or overprinting at the intersection of Zr-in-rutile temperatures and the retrograde

407   path for the LCU. Therefore, based on estimated *P-T* conditions of rutile growth from Groppo et al.

408   (2009) and constraints from Zr-in-rutile thermometry, a post-UHP timing of rutile growth can be

409   ruled out.

410   Here, quartz is present as inclusions in rutile and both zircon and coesite are present as

411   inclusions within the surrounding omphacite grains (Fig. 4). Although no zircon inclusions were

412   identified in the rutile, it has been established that zircon is an ubiquitous accessory mineral in the

413   mineral assemblage of the Lago di Cignana eclogites (King et al., 2004). Therefore, we can safely

414   assume that aSi = aZr = 1 during rutile growth, thereby satisfying the requirements for accurate Zr-

415   in-rutile thermometry. The pressure range of rutile growth was estimated to be 2.3–2.8 GPa based

416   on the quartz-coesite transition as an upper limit. The lower limit is based on the timing of rutile

417   growth relative to garnet growth, and *P-T* conditions obtained for the latter (Groppo et al., 2009).

418   The resulting temperature range of 510–565 (± 20) °C agrees with the prograde *P-T* conditions

419   determined by Groppo et al. (2009). Determining the timing of deformation of rutile and omphacite

420   is problematic due to a lack of constraints. However, deformation after the metamorphic peak was

421   limited, as exhumation coincided with the localization of deformation into shear bands (Van der

422   Klauw et al., 1997), which are lacking in the omphacite vein studied here.

423   The formation of Fe-platelets in rutile (Fig. 3b) is a common process that takes place in

424   response to exhumation and cooling (Putnis, 1978). This exsolution is an unmixing process that

425   reduces the energy of an oversaturated solution. Here, the presence of these Fe-bearing exsolution

426   products is explained by cooling associated with the rapid exhumation of this Alpine region after the

427   metamorphic peak at 45–41 Ma (Gouzu, Yagi, Thanh, Itaya & Compagnoni, 2016; Rubatto et al.,

428   1998; Amato et al., 1999; Reddy et al., 1999).

429   Before assessing the role of microstructures in the mobility of trace elements, volume

430   diffusion must be considered for reference (Fig. 11). Because the rate of bulk/volume diffusion is

431   exponentially temperature-dependent, the majority of diffusion will have taken place at (near-) peak

432   metamorphic temperature, which is 590–630 °C in the case of the LCU (Groppo et al., 2009;

433   Reinecke, 1998). An estimate of the duration of (near-) peak temperatures duration can be made

434   based on various geochronology data (Ssection 2.1). Relevant ages are compiled into an overview in

435   Figure 11a. Assuming 44 Ma as the onset of peak temperatures (Rubatto et al., 1998) and 36 Ma as

436   cooling below this temperature during exhumation (Reddy et al., 2003), the maximum duration of

437   (near-) peak temperature is 8 Myr supported by, Gouzu et al. (2016) who argue that peak conditions

438   lasted less than 5 Myr.

439

440   **5.2   Crystal-plastic deformation of rutile**

441   Intragranular distortion in rutile occurred by dislocation creep and resulted in the formation

442   of LABs within the crystal. For rutile, only a few studies report on natural deformation

443   microstructures (Moore et al., 2020; Plavsa, Reddy, Clark, & Agangi, 2018). However, the activation

444   of the slip systems in rutile has been studied experimentally since the early 1960s. These studies

445   revealed activation of the {101}<-101> and {110}<001> slip systems depending on crystal orientation

446   (Ashbee & Smallman, 1963; Hirthe & Brittain, 1963). Furthermore, Carr & Graham (1985,

447   unpublished data) described slip on the (100) plane. Later studies reportedactivation of the {101}<-

448   101> and {110}<001> slip systems to be temperature dependent with activation occurring at 600 °C

449   and 900 °C, respectively (Blanchin, Bursill, & Lafage, 1990), under experimental stresses and strain

450   rates. The presence of both these slip systems is also in agreement with experimental results on the

451   effect of indentation on the (001) (Basu, Elshrief, Coward, Anasori, & Barsoum, 2012). Furthermore,

452   results from a more recent study on natural rutile samples by Moore et al., (2020) demonstrated

453   that activation of {110}<001> can occur below 900 °C, presumably due to strain rates that are lower

454   in nature than in experiments.

455   The microstructural analysis of rutile by EBSD shows the presence of LABs with

456   misorientation axes parallel to <100> and <110>, indicating the presence of tilt walls formed by

457   climb of edge dislocations on the {100}<001> and {110}<001> slip system. Considering that M2 and

458   M5 were prepared from the same LAB, the multiple misorientation axes it show that this boundary

459 is segmented. . The UHP-LT (>2.7 GPA, ~600 °C) metamorphic conditions suggest that the

460 temperature threshold of ≤ 600°C for this slip system at typical natural stresses and strain rates

461 (Blanchin et al., 1990) is lower than indicated in early experimental studies. This would be in

462 agreement with the conclusion of Moore et al., (2020) on the {110}<001> slip system.

5.3　　　Formation of nanoscale substructures

464 　　　The LABs observed by EBSD were targeted for APT and TEM analyses, which revealed a

465 complex underlying substructure. Evenly spaced linear features lie consistently within the plane of

466 the LAB. The geometry, size, and spacing of these features suggests that they are dislocations and

467 are therefore intrinsic to the LAB (Hirthe & Balluffi, 1973). APT studies on LABs have previously

468 observed similar features in zircon (Piazolo et al., 2016; Reddy et al., 2016) and titanite (Kirkland et

469 al., 2018). In rutile, the geometry of linear features in the LAB is comparable with dislocations

470 observed in twin boundaries in rutile (Reddy et al., 2020, Verberne et al., 2022). The spacing

471 between dislocations, as well as the diameter of the zone of enrichment in trace-elements, varies

472 between the materials. The enriched zone consists of the dislocation core and a surrounding area of

473 lattice distorted by elastic strain and associated stresses, indicating that the enriched zone

474 constitutes a Cottrell atmosphere (Cottrell & Bilby, 1949). The capture of trace elements in the

475 Cottrell atmosphere reduces the stress fields. In minerals, studies by APT show that the enrichment

476 zone extends for approximately 3–5 nm in zircon (Piazolo et al., 2016) and, 10–24 nm in titanite

477 (Kirkland et al., 2018). In this study, dislocations in rutile have an enriched zone of trace elements of

478 8–10 nm in diameter, similar to the dislocations observed in twin boundaries (Reddy et al., 2020,

479 Verberne et al., 2022). Relative to their respective Burgers vector (*b*) these enriched zones have a

480 diameter of approximately 17*b*–33*b* in the rutile, 4*b*–8*b* in zircon, and 11*b*–33*b* in titanite, depending

481 on the direction of the Burgers vector. Modelling of Cottrell atmospheres in metallic samples (Ni)

482 with hydrogen as solute/trace element yields diameters of approximately 12*b* *(Sills & Cai, 2018)*. The

483 stress field around dislocations and difference in material could cause the difference for how far

484   from the core a Cottrell atmosphere can extend and put a limit on the maximum concentration of

485   trace elements around a dislocation (Cochardt, Schoek, & Wiedersich, 1955). Furthermore, the

486   difference in electric field around the dislocation and the host material in each mineral when

487   exposed during APT analysis and differences in reconstruction parameters could lead to a magnifying

488   effect on the observed radius of the Cottrell atmosphere.

489   The dislocations that form the LAB lie on a plane that is offset by intervals of approximately

490   10 nm, referred to as "steps" (Fig. 8b, 9c, d). Such a structure was not observed in previous APT

491   analyses of LABs in zircon (Piazolo et al., 2016; Reddy et al., 2016) and titanite (Kirkland et al., 2018).

492   The dislocations are still visible within these steps (Fig. 9c), suggesting that the steps formed during

493   crystal-plastic deformation or when the dislocations were pinned in place. It is unlikely that this

494   feature is a set of dislocations that is intersecting the LAB on a different slip system. This

495   configuration would not result in the offset of the LAB itself and the dimensions of this feature do

496   not fit with the other dislocations observed in this and previous studies of rutile (Verberne et al.,

497   2022, Reddy et al., 2020; Kuzmina, Herbig, Ponge, Sandlöbes, & Raabe, 2015)). Instead, this feature

498   is interpreted to reflect a long-period (chemical) stacking order (LPSO) ((Inoue, Kawamura,

499   Matsushita, Hayashi, & Koike, 2001). LPSO's are known in the material sciences and are formed as a

500   mechanism for strain accommodation in a chemically enriched region ((Abe, Kawamura, Hayashi, &

501   Inoue, 2002; Furuhara & Gu, 2013; Inoue et al., 2001). It is therefore expected that nucleation of

502   these structural sites occurs on an existing array of dislocations. The chemical ordering is then

503   achieved by the local strain field around the dislocations enhancing diffusion of trace elements (Abe

504   et al., 2002).

505   **5.4   Mechanisms for element mobility**

506

507   The diffusion of Zr through rutile parallel to the c-axis, the direction of fastest diffusion, has

508   been studied experimentally at temperatures in the range 750–1100 °C (Cherniak et al., 2007).

509   Extrapolation of the Arrhenius equation in Cherniak et al. (2007) gives the effective diffusion

510   distance for Zr in rutile over temperatures and durations representative of peak metamorphism of

511   the LCU (Fig. 11). For comparison, the effective diffusion distance is also given for Fe parallel and

512   perpendicular to the c-axis based on a temperature-dependent power law of experimentally

513   obtained diffusion coefficients by Sasaki et al. (1985). Fe diffuses several orders of magnitude faster

514   than Zr and, with an effective diffusion distance of 0.2–4.5 m, should be homogenised throughout

515   the rutile crystals. In contrast, the upper limit for the effective diffusion distance of Zr is

516   approximately 20 μm, thus limiting homogenization. Based on the work by Cherniak et al. (2007) and

517   Dohmen, Marschall, Ludwig, & Polednia (2019), the temperature at whichZr diffusion in rutile

518   becomes negligible for Zr-in-rutile thermometry is around 600–650 °C. This temperature range is in

519   agreement with the short effective diffusion distance for Zr estimated for the LCU. Al and Si, two

520   elements that are enriched within the LABs (Fig. 10), are experimentally demonstrated to diffuse

521   significantly slower than other elements in rutile at high temperature (Cherniak & Watson, 2019).

522   This difference in diffusivity also holds up when extrapolating diffusion coefficients to temperatures

523   relevant to the LCU (Fig. 11).

524   The presence of nanoscale substructures in the low-angle boundary that are chemically and

525   structurally different from each other suggest that different mechanisms for trace-element mobility

526   were potentially active at the same time. Low-angle boundaries form by stress-induced glide and

527   climb (Dhanaraj G, Byrappa K, Prasad V, Dudley 2010), therefore four main mechanisms need to be

528   evaluated, that is the effectiveness of volume diffusion and transport to the LAB, the potential for

529   fast-diffusion pathways or trace element trapping in dislocation, and the dislocation-impurity pair

530   migration. Previous APT studies

531   demonstrated that information on the active diffusion mechanisms could be derived from

532   the APT datasets and correlative analysis. Volume diffusion in combination with U-decay effects

533   results in the formation of Pb enriched clusters (Peterman et al., 2019; Peterman et al., 2016; Valley

534   et al., 2014; Valley et al., 2015; Verberne et al., 2020). Fast-diffusion pathways in the form of low-

535 and high-angle and twin boundaries allow for element migration (Denis Fougerouse et al., 2019; D.

536 Fougerouse et al., 2018; Piazolo et al., 2016), however these also have been shown to act as trace-

537 element traps (Verberne et al., 2022) and dislocation-impurity pair migration was suggested to lead

538 to trace-element enrichment in titanite (Kirkland et al., 2018) and pyrite (Dubosq et al., 2019).

539   Here, APT revealed that the features associated with the LAB are enriched in common trace

540 elements (e.g., Fe, Zr, Si, Al) and, in the case of the dislocations composing the LAB and one

541 orthogonal dislocation, also in uncommon Ca. The presence of Fe and other trace elements with an

542 affinity for rutile in the nanoscale substructure might reflect capture of trace elements in the strain

543 field around dislocations (Cottrell & Bilby, 1949). The models for volume diffusion (Fig. 11) indicate

544 that Fe and Zr both could diffuse into the dislocations during peak metamorphism. Subsequent

545 migration of dislocations into the LAB would result in enrichment of the LAB in trace elements

546 (Dubosq et al., 2019; Imai & Sumino, 1983; Petukhov & Klyuchnik, 2012). Alternatively, these

547 elements could be derived from the grain exterior (Fougerouse et al., 2019; Joesten, 1991; Kirkland

548 et al., 2018), which would result in a question regarding whether the dislocations behaved as an

549 element trap, as a pathway for diffusion, or both.

550

551   Besides trace elements that are common in rutile, the dislocations are decorated in Ca. Ca

552 has no affinity for rutile and is not expected to be incorporated within the crystal lattice during

553 growth. Reports on Ca in rutile attributed its apparent presence to potential interference with the

554 surrounding Ca-bearing silicate phases (Zack, Kronz, Foley, & Rivers, 2002). Rutile standards for LA-

555 ICP-MS, such as R10 (Luvizotto et al., 2009), also lack values for Ca calibration. LA-ICP-MS data in this

556 study (Supplementary data – DR3) generally did not indicate Ca in rutile above detection limits of

557 between 14 and 139 ppm. The lack of Ca in the rutile matrix rules out volume diffusion and

558 dislocation-impurity pair diffusion as mechanisms for Ca enrichment in dislocations. Besides Ca

559 enrichment around dislocations, volume diffusion would have resulted in enrichment of the rutile

560 matrix, and without Ca in the matrix no ions can be captured in the strain field of the dislocations.

561   The ionic sizes of elemental species in part control element migration, and therefore it can be

562   questioned whether large cations such as Ca can migrate into the region of elastic strain around a

563   dislocation from the matrix (Cottrell & Bilby, 1949; Kirkland et al., 2018; (Shannon, 1976).

564   The rutile grain resides within an omphacite vein also including apatite and glaucophane,

565   indicating that Ca was readily available during vein formation. The fluid from which the omphacite

566   vein formed is a probable source for the Ca, which was likely incorporated in the rutile by diffusion

567   along the LABs.

568   Si and Al are enriched in the LABs alongside Ca, but are more readily incorporated in rutile

569   and thus do not require an external source (Fig. 5). However, Si and Al are known to migrate by

570   volume diffusion at significantly lower rates in rutile than other elements (Fig. 11; Cherniak and

571   Watson, 2019). The affinity of these elements for LABs without the possibility for their enrichment

572   through volume diffusion at the temperature and timescale of the LCU, indicates a different

573   mechanism of incorporation. This mechanism could be similar to Ca, namely incorporation and

574   transport from an external source into the grain interior along LABs, or otherwise dislocation-

575   impurity migration.

576   Trace-element enrichment by fast diffusion along dislocations, or "pipe" diffusion (Love,

577   1964), has been suggested in previous APT studies on minerals to facilitate the removal of Pb in

578   zircon (Piazolo et al., 2016) or allow for the incorporation of K, a large cation, in titanite (Kirkland et

579   al., 2018). Therefore, we interpret the Ca decorating the dislocations in rutile as externally derived

580   and to have been incorporated into the low-angle boundary by enhanced diffusivity along

581   dislocations.

582   The lack of Ca in one of the vertically orientated dislocations and the steps (Fig. 9, 10),

583   further suggests that Ca incorporation predated these dislocations or was energetically

584   unfavourable. Migrating dislocations can be entangled, resulting in core-core and overlap leading to

585   enrichment in trace elements, as demonstrated for pyrite (Fougerouse et al., 2019). Here, the

586   simplest explanation would be that a migrating dislocation becomes entangled and pinned on the

587   pre-existing Ca-rich dislocations. The lack of Ca in the Ca-free dislocation suggests that diffusion of

588   large cations like Ca became ineffective before this entanglement.

589   The impact of intragranular substructure on rates of diffusion needs to be considered as

590   dislocations can act as fast diffusion pathways or traps for trace elements. An effective diffusion

591   distance of 10 µm (Fig. 11) allows for the mobilization of Zr into the LAB network for much of the

592   grain interior (Fig. 6). The question becomes whether Zr is retained or mobilized along the

593   dislocations. Recent APT studies on rutile show that while Zr might be able to migrate along

594   dislocations, the diffusivity of Zr along dislocations is still slow (Verberne et al., 2022). It was

595   therefore suggested that dislocations mainly act as a trap for mobile Zr, thus preserving bulk Zr

596   concentrations, albeit in a more localised form.

597

598   Trace-element enrichment is highest in the dislocation cores, with lower concentrations of

599   impurities further away from the dislocation cores. This distribution is consistent with observations

600   of H in Ni (Sills & Cai, 2018). In the 'steps' and where the entangled dislocations intersect, the

601   difference in concentration between the rutile matrix and features is approximately 6 at. %. While

602   not matching a known different mineral phase, a 6 at. % difference in composition raises the

603   question whether these features should be considered rutile or a discrete, thermodynamically stable

604   phase? Similar features, though in higher concentrations, have been described as linear complexions

605   (Kuzmina et al., 2015).

606   **5.5   Implications for Zr-in-rutile geothermometry**

607

608   he influence of Zr present within a LAB on composition measurements by various techniques

609   can be predicted (Fig. 12), although it remains an open question as to whether Zr is retained or

610   migrates along dislocations. Figure 12 shows the modelled results for Zr-in-rutile thermometry that

611   would be obtained by techniques with different spatial resolution and plots the atomic

612 concentration of Zr against temperature. Zr-in-rutile thermometry is calibrated for the Zr

613 concentration in weight percentages. Thus, the substitution of Ti and O for any other element will

614 barely affect the measured Zr concentration. Here, it is shown that dislocations and other

615 substructures linked to the LAB can result in the exchange of 1–8 at. % Ti for other trace elements

616 (Fig. 10). However, this compositional modification is very localised. Hence, the spatial resolution of

617 the analytical technique used for measuring Zr concentration may play a critical role in determining

618 the measured concentrations. In Figure 12, we assess the influence of the spatial resolutions of

619 different techniques on Zr-in-rutile thermometry under the following assumptions:

620   1.   The chemical system is simplified assuming a composition of $Ti_{1-x}O_2$, where x is only Zr.

621   2.   The Zr concentration in the LAB is based on the proximity diagram of this study (0.01 at. %)

622   3.   "Measurements" are acquired on surfaces perpendicular to the LAB and are centred on the

623   LAB.

624   4.   The length and depth of the LAB are equal to the spot size (*d*) diameters and analytical

625   depth. The width of the LAB is equal to the diameter of the zone of chemical enrichment

626   around dislocations (*y*) visualized by APT.

627   5.   The volume of the LAB within the spot analysis is simplified to be *length (l)*width (w)*depth*

628   *(h)*, ignoring the curvature at the edges.

629   6.   The apparent composition of the LAB is a mix between the composition of the dislocations

630   and that of the remaining volume in the LAB assumed to have the composition of the matrix.

631   The contributions of dislocations and matrix to the composition of the LAB are set to 50%

632   each based on the isoconcentration profiles of Specimens 1 and 2 (Fig. 9).

633 From the above assumptions the proportion of matrix sampled by a given spot size is:

634 $\left(1 - \frac{4y}{\pi d}\right)$ (eq. 1).

635 Assuming that the matrix Zr concentration represents the "true value" (Fig. 12) the red line indicates

636 the expected temperature for a given concentration. The other profiles represent the measurements

637 based on analysis with different spot sizes, measuring a volume that contains a Zr-enriched LAB. The

638   smaller analytical volumes measure relatively less matrix. With increasing temperature, these

639   temperature profiles converge to the point where the concentration of Zr in dislocations matches

640   the concentration of Zr in the matrix. At even higher concentrations of Zr in the matrix, the

641   profilesThese woulddiverge as a lower Zr concentration in the LAB compared to the matrix would

642   lead to a lower estimate of the temperature.

643   Here, we observed an enrichment of Zr in the LAB's. Zr-in-rutile temperatures calculated from

644   analyses performed with a spot size >1 µm are not influenced by the Zr enrichment of the LAB due

645   to the volume of matrix material measured being far greater than the volume of dislocations. For the

646   measurements performed in this study, LA-ICP-MS with a 50 µm spot size, the temperatures are

647   representative. Analytical techniques with spot sizes less than 1 µm overestimate the temperature,

648   becoming more significant around a spot size of 200nm. If it is assumed Zr was removed from the

649   rutile via the LAB network, spot sizes <1 µm might provide more accurate Zr-in-rutile temperatures if

650   the beam intersects a subgrain boundary. However, current models are not calibrated for the

651   properties of dislocations.

652   Based on the work done in this study, the demonstration of trapping of Zr and the literature (Clark et

653   al., 2019), it is again clear that Zr-in-rutile geothermometry is a robust technique, including at low

654   temperatures and (U)HP conditions. Analytical techniques with a relatively low spatial resolution

655   such as LA-ICP-MS are ideal for the measurement of Zr concentration. However, when it can be

656   demonstrated that diffusion caused the loss of Zr via bulk diffusion, high spatial resolution

657   techniques incorporating microstructures could provide more accurate results or a better range of

658   temperature estimate because of the trapping of Zr in dislocations.

659   **6. SUMMARY**

660   The rutile analysed in this study records prograde growth, and was thereafter incorporated in a

661   peak-metamorphic omphacite vein that formed at ultra-high pressure conditions. The rutile was

662   deformed in between these two events, resulting in the formation of low-angle boundaries by

663 dislocations predominantly on the {100}[001] slip systems. The dislocations that constitute the low-

664 angle boundary are enriched in trace elements and form several structures as revealed in the 3D APT

665 data. Fe, Ca, Zr, Al and Si are found at elevated concentrations in these boundaries. The enrichment

666 of those elements except Fe cannot be explained by solely assuming volume diffusion. Pipe diffusion

667 via these deformation structures likely played a role in the redistribution of trace elements,

668 potentially from the grain exterior in case of Ca. The enrichment of low-angle boundaries needs to

669 be considered when applying geochemistry to deformed minerals, as it can lead to faster re-

670 equilibration by diffusion, and it can affect measurements targeting the crystal matrix. Measuring

671 trace element concentrations (e.g., Zr) by techniques with high-spatial resolution can lead to

672 significant overestimations of the concentration compared to bulk (>50 °C for Zr-in-rutile).

673 **7. ACKNOWLEDGMENTS**

685

686

687 **8. REFERENCES**

688 Abe, E., Kawamura, Y., Hayashi, K., & Inoue, A. (2002). Long-period ordered structure in a high-
689   strength nanocrystalline Mg-1 at% Zn-2 at% Y alloy studied by atomic-resolution Z-contrast
690   STEM. *Acta Materialia, 50*(15), 3845-3857. doi:https://doi.org/10.1016/S1359-
691   6454(02)00191-X

692 Amato, J.M., Johnson, C.M., Baumgartner, L.P., and Beard, B.L., 1999, Rapid exhumation of the
693   Zermatt-Saas ophiolite deduced from high-precision Sm–Nd and Rb–Sr geochronology: Earth
694   and Planetary Science Letters, v. 171, p. 425–438.

695 Ashbee, K., & Smallman, R. E. (1963). The plastic deformation of titanium dioxide single crystals.
696   *Proceedings of the Royal Society of London. Series A. Mathematical and Physical Sciences,*
697   *274*(1357), 195-205.

698 Bachmann, F., Hielscher, R., & Schaeben, H. (2010). *Texture analysis with MTEX–free and open*
699   *source software toolbox.* Paper presented at the Solid State Phenomena.

700 Basu, S., Elshrief, O. A., Coward, R., Anasori, B., & Barsoum, M. W. (2012). Microscale deformation of
701   (001) and (100) rutile single crystals under spherical nanoindentation. *Journal of Materials*
702   *Research, 27*(1), 53.

703 Blanchin, M., Bursill, L., & Lafage, C. (1990). Deformation and microstructure of rutile. *Proceedings of*
704   *the Royal Society of London. A. Mathematical and Physical Sciences, 429*(1876), 175-202.

705 Blum, T. B., Darling, J. R., Kelly, T. F., Larson, D. J., Moser, D. E., Perez-Huerta, A., . . . Saxey, D. W.
706   (2018). Best practices for reporting atom probe analysis of geological materials.
707   *Microstructural Geochronology: Planetary Records Down to Atom Scale, 232*, 369-373.

708 Cherniak, D. (2000). Pb diffusion in rutile. *Contributions to Mineralogy and Petrology, 139*(2), 198-
709   207.

710 Cherniak, D. J., Manchester, J., & Watson, E. B. (2007). Zr and Hf diffusion in rutile. *Earth and*
711   *Planetary Science Letters, 261*(1-2), 267-279. doi:10.1016/j.epsl.2007.06.027

712 Cherniak, D. J., & Watson, E. B. (2019). Al and Si diffusion in rutile. *American Mineralogist: Journal of*
713   *Earth and Planetary Materials, 104*(11), 1638-1649.

714   Crameri, F., 2018. Scientific colour-maps. Zenodo. http://doi.org/10.5281/zenodo.1243862

715   Cochardt, A., Schoek, G., & Wiedersich, H. (1955). Interaction between dislocations and interstitial

716   atoms in body-centered cubic metals. *Acta Metallurgica, 3*(6), 533-537.

717   Cottrell, A. H., & Bilby, B. (1949). Dislocation theory of yielding and strain ageing of iron. *Proceedings*

718   *of the Physical Society. Section A, 62*(1), 49.

719   Cutts, J., & Smit, M. (2018). Rates of deep continental burial from Lu-Hf garnet chronology and Zr-in-

720   rutile thermometry on (ultra) high-pressure rocks. *Tectonics, 37*(1), 71-88.

721   Dachille, F., Simons, P., & Roy, R. (1968). Pressure-temperature studies of anatase, brookite, rutile

722   and TiO2-II. *Am Mineral, 53*, 1929-1939.

723   Dhanaraj, G., Byrappa, K., Prasad, V. V., & Dudley, M. (2010). Crystal growth techniques and

724   characterization: an overview. Springer Handbook of Crystal Growth, 3-16.

725   DesOrmeau, J. W., Gordon, S. M., Little, T. A., Bowring, S. A., & Chatterjee, N. (2017). Rapid time

726   scale of Earth's youngest known ultrahigh-pressure metamorphic event, Papua New Guinea.

727   *Geology, 45*(9), 795-798.

728   Dohmen, R., Marschall, H. R., Ludwig, T., & Polednia, J. (2019). Diffusion of Zr, Hf, Nb and Ta in rutile:

729   effects of temperature, oxygen fugacity, and doping level, and relation to rutile point defect

730   chemistry. *Physics and Chemistry of Minerals, 46*(3), 311-332.

731   Dubosq, R., Rogowitz, A., Schweinar, K., Gault, B., & Schneider, D. A. (2019). A 2D and 3D

732   nanostructural study of naturally deformed pyrite: assessing the links between trace

733   element mobility and defect structures. *Contributions to Mineralogy and Petrology, 174*(9),

734   72.

735   Forster, M., Lister, G., Compagnoni, R., Giles, D., Hills, Q., Betts, P., . . . Tamagno, E. (2004). Mapping

736   of oceanic crust with" HP" to" UHP" metamorphism: The Lago di Cignana Unit,(Western

737   Alps). In *Mapping geology in Italy*: Geological Society of London.

738   Fougerouse, D., Reddy, S. M., Aylmore, M., Yang, L., Guagliardo, P., Saxey, D. W., . . . Timms, N.

739   (2021). A new kind of invisible gold in pyrite hosted in deformation-related dislocations.

740   *Geology, 49*(10), 1225-1229.

741   Fougerouse, D., Reddy, S. M., Kirkland, C. L., Saxey, D. W., Rickard, W. D., & Hough, R. M. (2019).

742   Time-resolved, defect-hosted, trace element mobility in deformed Witwatersrand pyrite.

743   *Geoscience Frontiers, 10(1)*, 55-63.

744   Fougerouse, D., Reddy, S. M., Saxey, D. W., Erickson, T. M., Kirkland, C. L., Rickard, W. D. A., . . .

745   Buick, I. S. (2018). Nanoscale distribution of Pb in monazite revealed by atom probe

746   microscopy. *Chemical Geology, 479*, 251-258.

747   doi:https://doi.org/10.1016/j.chemgeo.2018.01.020

748   Fougerouse, D., Saxey, D. W., Rickard, W. D., Reddy, S. M., & Verberne, R. (2021). Standardizing

749   Spatial Reconstruction Parameters for the Atom Probe Analysis of Common Minerals.

750   *Microscopy and Microanalysis*, 1-10.

751   Frezzotti, M., Selverstone, J., Sharp, Z., & Compagnoni, R. (2011). Carbonate dissolution during

752   subduction revealed by diamond-bearing rocks from the Alps. *Nature Geoscience, 4*(10),

753   703-706.

754   Furuhara, T., & Gu, X. (2013). Discussion on strain accommodation associated with formation of

755   LPSO Structure. *Materials Transactions, 54*(5), 675-679.

756   Gao, X. Y., Zheng, Y. F., Xia, X. P., & Chen, Y. X. (2014). U-Pb ages and trace elements of metamorphic

757   rutile from ultrahigh-pressure quartzite in the Sulu orogen. *Geochimica Et Cosmochimica*

758   *Acta, 143*, 87-114. doi:10.1016/j.gca.2014.04.032

759   Gault, B., Moody, M. P., Cairney, J. M., & Ringer, S. P. (2012). *Atom probe microscopy* (Vol. 160):

760   Springer Science & Business Media.

761   Groppo, C., Beltrando, M., & Compagnoni, R. (2009). The P–T path of the ultra-high pressure Lago Di

762   Cignana and adjoining high-pressure meta-ophiolitic units: insights into the evolution of the

763   subducting Tethyan slab. *Journal of Metamorphic Geology, 27*(3), 207-231.

764 Gouzu, C., Yagi, K., Thanh, N. X., Itaya, T., and Compagnoni, R., 2016, White mica K–Ar

765   geochronology of HP–UHP units in the Lago di Cignana area, western Alps, Italy: tectonic

766   implications for exhumation: Lithos, v. 248, p. 109-118.

767 Halama, R., Konrad-Schmolke, M., & De Hoog, J. C. (2020). Boron isotope record of peak

768   metamorphic ultrahigh-pressure and retrograde fluid–rock interaction in white mica (Lago di

769   Cignana, Western Alps). *Contributions to Mineralogy and Petrology, 175*(3), 20.

770 Hart, E., Storey, C., Bruand, E., Schertl, H. P., & Alexander, B. D. (2016). Mineral inclusions in rutile: A

771   novel recorder of HP-UHP metamorphism. *Earth and Planetary Science Letters, 446*, 137-

772   148. doi:10.1016/j.epsl.2016.04.035

773 Hart, E., Storey, C., Harley, S. L., & Fowler, M. (2018). A window into the lower crust: Trace element

774   systematics and the occurrence of inclusions/intergrowths in granulite-facies rutile.

775   *Gondwana Research, 59*, 76-86. doi:10.1016/j.gr.2018.02.021

776 Hellman, O. C., Vandenbroucke, J. A., Rusing, J., Isheim, D., & Seidman, D. N. (2000). Analysis of

777   Three-dimensional Atom probe Data by the Proximity Histogram. *Microsc Microanal, 6*(5),

778   437-444. doi:10.1017.S1431927600000635

779 Hirthe, W. M., & Brittain, J. O. (1963). High-Temperature Steady-State Creep in Rutile. *Journal of the

780   American Ceramic Society, 46*(9), 411-417.

781 Hirth, J. P., & Balluffi, R. W. (1973). On grain boundary dislocations and ledges. Acta Metallurgica,

782   21(7), 929-942.

783 Imai, M., & Sumino, K. (1983). In situ X-ray topographic study of the dislocation mobility in high-

784   purity and impurity-doped silicon crystals. *Philosophical Magazine A, 47*(4), 599-621.

785 Inoue, A., Kawamura, Y., Matsushita, M., Hayashi, K., & Koike, J. (2001). Novel hexagonal structure

786   and ultrahigh strength of magnesium solid solution in the Mg–Zn–Y system. *Journal of

787   Materials Research, 16*(7), 1894-1900. doi:10.1557/JMR.2001.0260

788   Jamieson, J. C., & Olinger, B. (1969). Pressure-temperature studies of anatase, brookite rutile, and

789   Ti02 (II): A discussion. *American Mineralogist: Journal of Earth and Planetary Materials, 54*(9-

790   10), 1477-1481.

791   Joesten, R. (1991). Grain-boundary diffusion kinetics in silicate and oxide minerals. In *Diffusion,*

792   *atomic ordering, and mass transport* (pp. 345-395): Springer.

793   Keller, L. M., Abart, R., Wirth, R., Schmid, D. W., & Kunze, K. (2006). Enhanced mass transfer through

794   short-circuit diffusion: growth of garnet reaction rims at eclogite facies conditions. *American*

795   *Mineralogist, 91*(7), 1024-1038.

796   King, R. L., Bebout, G. E., Kobayashi, K., Nakamura, E., & Van Der Klauw, S. N. (2004). Ultrahigh-

797   pressure metabasaltic garnets as probes into deep subduction zone chemical cycling.

798   *Geochemistry, Geophysics, Geosystems, 5*(12).

799   Kirkland, C., Fougerouse, D., Reddy, S., Hollis, J., & Saxey, D. (2018). Assessing the mechanisms of

800   common Pb incorporation into titanite. *Chemical Geology, 483*, 558-566.

801   Kirst, F., & Leiss, B. (2017). Kinematics of syn-and post-exhumational shear zones at Lago di Cignana

802   (Western Alps, Italy): constraints on the exhumation of Zermatt–Saas (ultra) high-pressure

803   rocks and deformation along the Combin Fault and Dent Blanche Basal Thrust. *International*

804   *Journal of Earth Sciences, 106*(1), 215-236.

805   Klinger, L., & Rabkin, E. (1999). Beyond the Fisher model of grain boundary diffusion: effect of

806   structural inhomogeneity in the bulk. *Acta Materialia, 47*(3), 725-734.

807   Kohn, M. J. (2020). A refined zirconium-in-rutile thermometer. *American Mineralogist: Journal of*

808   *Earth and Planetary Materials, 105*(6), 963-971.

809   Kooijman, E., Mezger, K., & Berndt, J. (2010). Constraints on the U-Pb systematics of metamorphic

810   rutile from in situ LA-ICP-MS analysis. *Earth and Planetary Science Letters, 293*(3-4), 321-330.

811   doi:10.1016/j.epsl.2010.02.047

812   Kuzmina, M., Herbig, M., Ponge, D., Sandlöbes, S., & Raabe, D. (2015). Linear complexions: confined

813   chemical and structural states at dislocations. *Science, 349*(6252), 1080-1083.

814   Lapen, T.J., Johnson, C.M., Baumgartner, L.P., Mahlen, N.J., Beard, B.L., Amato, J.M., (2003). Burial

815   rates during prograde metamorphism of an ultra-high-pressure terrane: an example from

816   Lago di Cignana, western Alps, Italy. Earth and Planetary Science Letters, 215, 57-72

817   Larson, D. J., Prosa, T. J., Ulfig, R. M., Geiser, B. P., & Kelly, T. F. (2013). Local electrode atom probe

818   tomography. *NY: Springer, New York*.

819   Love, G. (1964). Dislocation pipe diffusion. *Acta Metallurgica, 12*(6), 731-737.

820   Lund, M. D., Piazolo, S., & Harley, S. L. (2006). Ultrahigh temperature deformation microstructures in

821   felsic granulites of the Napier Complex, Antarctica. Tectonophysics, 427(1-4), 133-151.

822   Luvizotto, G. L., Zack, T., Meyer, H. P., Ludwig, T., Triebold, S., Kronz, A., . . . von Eynatten, H. (2009).

823   Rutile crystals as potential trace element and isotope mineral standards for microanalysis.

824   *Chemical Geology, 261*(3-4), 346-369. doi:10.1016/j.chemgeo.2008.04.012

825   Mei, Z. G., Wang, Y., Shang, S. L., & Liu, Z. K. (2014). First-principles study of the mechanical

826   properties and phase stability of TiO2. *Computational Materials Science, 83*, 114-119.

827   doi:10.1016/j.commatsci.2013.11.020

828   Mezger, K., Hanson, G., & Bohlen, S. (1989). High-precision UPb ages of metamorphic rutile:

829   application to the cooling history of high-grade terranes. *Earth and Planetary Science Letters,*

830   *96*(1-2), 106-118.

831   Montalvo, S. D., Reddy, S. M., Saxey, D. W., Rickard, W. D. A., Fougerouse, D., Quadir, Z., & Johnson,

832   T. E. (2019). Nanoscale constraints on the shock-induced transformation of zircon to reidite.

833   *Chemical Geology, 507*, 85-95. doi:https://doi.org/10.1016/j.chemgeo.2018.12.039

834   Moore, J., Beinlich, A., Porter, J. K., Talavera, C., Berndt, J., Piazolo, S., . . . Putnis, A. (2020).

835   Microstructurally controlled trace element (Zr, U–Pb) concentrations in metamorphic rutile:

836   An example from the amphibolites of the Bergen Arcs. *Journal of Metamorphic Geology,*

837   *38*(1), 103-127.

838   Müller, W. F., & Compagnoni, R. (2009). Eclogite from the ultrahigh-pressure metamorphic unit at

839   Lago di Cignana, Western Alps: A process-oriented transmission electron microscope study.

840   *Lithos, 109*(3-4), 323-332.

841   Ni, P., Zhu, X., Wang, R., Shen, K., Zhang, Z., Qiu, J., & Huang, J. (2008). Constraining ultrahigh-

842   pressure (UHP) metamorphism and titanium ore formation from an infrared

843   microthermometric study of fluid inclusions in rutile from Donghai UHP eclogites, eastern

844   China. *Geological Society of America Bulletin, 120*(9-10), 1296-1304.

845   Norman, M., Pearson, N., Sharma, A., & Griffin, W. (1996). Quantitative analysis of trace elements in

846   geological materials by laser ablation ICPMS: instrumental operating conditions and

847   calibration values of NIST glasses. *Geostandards Newsletter, 20*(2), 247-261.

848   Oberti, R., & Caporuscio, F. A. (1991). Crystal chemistry of clinopyroxenes from mantle eclogites: a

849   study of the key role of the M2 site population by means of crystal-structure refinement.

850   *American Mineralogist, 76*(7-8), 1141-1152.

851   Pearce, N. J., Perkins, W. T., Westgate, J. A., Gorton, M. P., Jackson, S. E., Neal, C. R., & Chenery, S. P.

852   (1997). A compilation of new and published major and trace element data for NIST SRM 610

853   and NIST SRM 612 glass reference materials. *Geostandards Newsletter, 21*(1), 115-144.

854   Peterman, E., Reddy, S. M., Saxey, D., Fougerouse, D., Snoeyenbos, D., & Rickard, W. (2019).

855   Nanoscale processes of trace element mobility in metamorphosed zircon. *Contributions to

856   Mineralogy and Petrology, 174*(11), 92.

857   Peterman, E. M., Reddy, S. M., Saxey, D. W., Snoeyenbos, D. R., Rickard, W. D., Fougerouse, D., &

858   Kylander-Clark, A. R. (2016). Nanogeochronology of discordant zircon measured by atom

859   probe microscopy of Pb-enriched dislocation loops. *Sci Adv, 2*(9), e1601318.

860   doi:10.1126/sciadv.1601318

861   Petukhov, B., & Klyuchnik, P. (2012). Dynamic interaction of dislocations with impurity subsystem in

862   crystalline materials. *Crystallography Reports, 57*(3), 388-392.

863   Piazolo, S., La Fontaine, A., Trimby, P., Harley, S., Yang, L., Armstrong, R., & Cairney, J. M. (2016).

864   Deformation-induced trace element redistribution in zircon revealed using atom probe

865   tomography. *Nature communications, 7*(1), 1-7.

866   Plavsa, D., Reddy, S. M., Clark, C., & Agangi, A. (2018). *Capricorn Orogen rutile study, a combined*

867   *electron backscatter diffracction (EBSD) and laser ablation split stream (LASS) analytical*

868   *approach, Record 2018/12, 54p*. Retrieved from

869   Plümper, O., King, H. E., Vollmer, C., Ramasse, Q., Jung, H., & Austrheim, H. (2012). The legacy of

870   crystal-plastic deformation in olivine: high-diffusivity pathways during serpentinization.

871   *Contributions to Mineralogy and Petrology, 163*(4), 701-724.

872   Putnis, A. (1978). The mechanism of exsolution of hematite from iron-bearing rutile. *Physics and*

873   *Chemistry of Minerals, 3*(2), 183-197.

874   Recnik, A., Stankovic, N., & Daneu, N. (2015). Topotaxial reactions during the genesis of oriented

875   rutile/hematite intergrowths from Mwinilunga (Zambia). *Contributions to Mineralogy and*

876   *Petrology, 169*(2). doi:ARTN 1910.1007/s00410-015-1107-x

877   Reddy, S., Wheeler, J., & Cliff, R. (1999). The geometry and timing of orogenic extension: an example

878   from the Western Italian Alps. *Journal of Metamorphic Geology, 17*, 573-590.

879   Reddy, S. M., Saxey, D. W., Rickard, W. D., Fougerouse, D., Montalvo, S. D., Verberne, R., & Van

880   Riessen, A. (2020). Atom Probe Tomography: Development and Application to the

881   Geosciences. *Geostandards and Geoanalytical Research, 44*(1), 5-50.

882   Reddy, S. M., Timms, N. E., Pantleon, W., & Trimby, P. (2007). Quantitative characterization of plastic

883   deformation of zircon and geological implications. *Contributions to Mineralogy and*

884   *Petrology, 153*(6), 625-645. doi:10.1007/s00410-006-0174-4

885   Reddy, S. M., Timms, N. E., Trimby, P., Kinny, P. D., Buchan, C., & Blake, K. (2006). Crystal-plastic

886   deformation of zircon: A defect in the assumption of chemical robustness. *Geology, 34*(4),

887   257-260. doi:10.1130/G22110.1

888 Reddy, S. M., van Riessen, A., Saxey, D. W., Johnson, T. E., Rickard, W. D. A., Fougerouse, D., . . .

889   Olson, D. (2016). Mechanisms of deformation-induced trace element migration in zircon

890   resolved by atom probe and correlative microscopy. *Geochimica Et Cosmochimica Acta, 195*,

891   158-170. doi:10.1016/j.gca.2016.09.019

892 Reinecke, T. (1998). Prograde high-to ultrahigh-pressure metamorphism and exhumation of oceanic

893   sediments at Lago di Cignana, Zermatt-Saas Zone, western Alps. *Lithos, 42*(3-4), 147-189.

894 Rickard, W. D., Reddy, S. M., Saxey, D. W., Fougerouse, D., Timms, N. E., Daly, L., . . . Jourdan, F.

895   (2020). Novel Applications of FIB-SEM-Based ToF-SIMS in Atom Probe Tomography

896   Workflows. *Microscopy and Microanalysis*, 1-8.

897 Rocholl, A. B., Simon, K., Jochum, K. P., Bruhn, F., Gehann, R., Kramar, U., . . . Seufert, M. (1997).

898   Chemical Characterisation of NIST Silicate Glass Certified Reference Material SRM 610 by

899   ICP-MS, TIMS, LIMS, SSMS, INAA, AAS and PIXE. *Geostandards Newsletter, 21*(1), 101-114.

900 Rubatto, D., Gebauer, D., & Fanning, M. (1998). Jurassic formation and Eocene subduction of the

901   Zermatt–Saas-Fee ophiolites: implications for the geodynamic evolution of the Central and

902   Western Alps. *Contributions to Mineralogy and Petrology, 132*(3), 269-287.

903 Saxey, D., Moser, D., Piazolo, S., Reddy, S., & Valley, J. (2018). Atomic worlds: Current state and

904   future of atom probe tomography in geoscience. *Scripta Materialia, 148*, 115-121.

905 Sayle, D., Catlow, C., Perrin, M., & Nortier, P. (1995). Computer simulation study of the defect

906   chemistry of rutile TiO2. *Journal of Physics and Chemistry of Solids, 56*(6), 799-805.

907 Seydoux-Guillaume, A.-M., Fougerouse, D., Laurent, A., Gardés, E., Reddy, S., & Saxey, D. (2019).

908   Nanoscale resetting of the Th/Pb system in an isotopically-closed monazite grain: A

909   combined atom probe and transmission electron microscopy study. *Geoscience Frontiers,*

910   *10*(1), 65-76.

911 Shannon, R. D. (1976). Revised effective ionic radii and systematic studies of interatomic distances in

912   halides and chalcogenides. *Acta crystallographica section A: crystal physics, diffraction,*

913   *theoretical and general crystallography, 32*(5), 751-767.

914   Sills, R., & Cai, W. (2018). Free energy change of a dislocation due to a Cottrell atmosphere.

915   *Philosophical Magazine, 98*(16), 1491-1510.

916   Skora, S., Mahlen, N., Johnson, C. M., Baumgartner, L. P., Lapen, T., Beard, B. L., & Szilvagyi, E.

917   (2015). Evidence for protracted prograde metamorphism followed by rapid exhumation of

918   the Zermatt-Saas Fee ophiolite. *Journal of Metamorphic Geology, 33*(7), 711-734.

919   Smye, A. J., & Stockli, D. F. (2014). Rutile U-Pb age depth profiling: A continuous record of

920   lithospheric thermal evolution. *Earth and Planetary Science Letters, 408*, 171-182.

921   doi:10.1016/j.epsl.2014.10.013

922   Sutton, A. P., Balluffi, R. W., & Sutton, A. (1995). Interfaces in crystalline materials.

923   Swope, R. J., Smyth, J. R., & Larson, A. C. (1995). H in rutile-type compounds: I. Single-crystal neutron

924   and X-ray diffraction study of H in rutile. *American Mineralogist, 80*(5-6), 448-453.

925   Timms, N. E., Kinny, P. D., & Reddy, S. M. (2006). Enhanced diffusion of uranium and thorium linked

926   to crystal plasticity in zircon. *Geochemical Transactions, 7*(1), 10.

927   Timms, N. E., Kinny, P. D., Reddy, S. M., Evans, K., Clark, C., & Healy, D. (2011). Relationship among

928   titanium, rare earth elements, U–Pb ages and deformation microstructures in zircon:

929   Implications for Ti-in-zircon thermometry. *Chemical Geology, 280*(1-2), 33-46.

930   Tomkins, H. S., Powell, R., & Ellis, D. J. (2007). The pressure dependence of the zirconium-in-rutile

931   thermometer. *Journal of Metamorphic Geology, 25*(6), 703-713. doi:10.1111/j.1525-

932   1314.2007.00724.x

933   Valley, J. W., Cavosie, A. J., Ushikubo, T., Reinhard, D. A., Lawrence, D. F., Larson, D. J., . . . Moser, D.

934   E. (2014). Hadean age for a post-magma-ocean zircon confirmed by atom-probe

935   tomography. *Nature Geoscience, 7*(3), 219-223.

936   Valley, J. W., Reinhard, D. A., Cavosie, A. J., Ushikubo, T., Lawrence, D. F., Larson, D. J., . . . Strickland,

937   A. (2015). Nano- and micro-geochronology in Hadean and Archean zircons by atom-probe

938   tomography and SIMS: New tools for old minerals. *American Mineralogist, 100*(7), 1355-

939   1377. doi:10.2138/am-2015-5134

940 Van Actherbergh, E. (2001). Data reduction software for LA-ICP-MS. *Laser Ablation-ICP-mass*

941   *spectrometry in the earth sciences: principles and applications*, 239-243.

942 Van der Klauw, S., Reinecke, T., & Stöckhert, B. (1997). Exhumation of ultrahigh-pressure

943   metamorphic oceanic crust from Lago di Cignana, Piemontese zone, western Alps: the

944   structural record in metabasites. *Lithos, 41*(1-3), 79-102.

945 Verberne, R., Reddy, S., Saxey, D., Fougerouse, D., Rickard, W., Plavsa, D., . . . Kylander-Clark, A.

946   (2020). The geochemical and geochronological implications of nanoscale trace-element

947   clusters in rutile. *Geology*.

948 Verberne, R., Saxey, D. W., Reddy, S. M., Rickard, W. D., Fougerouse, D., & Clark, C. (2019). Analysis

949   of Natural Rutile (TiO2) by Laser-assisted Atom Probe Tomography. *Microscopy and*

950   *Microanalysis*, 1-8.

951 Verberne, R., Reddy, S. M., Saxey, D. W., Fougerouse, D., Rickard, W. D., Quadir, Z., ... & Clark, C.

952   (2022). Dislocations in minerals: Fast-diffusion pathways or trace-element traps?. Earth and

953   Planetary Science Letters, 584, 117517.

954 Vukmanovic, Z., Reddy, S. M., Godel, B., Barnes, S. J., Fiorentini, M. L., Barnes, S. J., & Kilburn, M. R.

955   (2014). Relationship between microstructures and grain-scale trace element distribution in

956   komatiite-hosted magmatic sulphide ores. *Lithos, 184*, 42-61.

957   doi:10.1016/j.lithos.2013.10.037

958 Watson, E. B., Wark, D. A., & Thomas, J. B. (2006). Crystallization thermometers for zircon and rutile.

959   *Contributions to Mineralogy and Petrology, 151*(4), 413-433. doi:10.1007/s00410-006-0068-

960   5

961 Whitney, D.L., Evans, B.W., 2010. Abbreviations for names of rock-forming minerals. American

962   Mineralogist, 95, 185-197

963 Withers, A. C., Essene, E. J., & Zhang, Y. X. (2003). Rutile/TiO2II phase equilibria. *Contributions to*

964   *Mineralogy and Petrology, 145*(2), 199-204. doi:10.1007/s00410-003-0445-2

965   Zack, T., & Kooijman, E. (2017). Petrology and geochronology of rutile. *Reviews in Mineralogy and*

966   *Geochemistry, 83*(1), 443-467.

967   Zack, T., Kronz, A., Foley, S. F., & Rivers, T. (2002). Trace element abundances in rutiles from

968   eclogites and associated garnet mica schists. *Chemical Geology, 184*(1-2), 97-122. doi:Pii

969   S0009-2541(01)00357-6

970   Doi 10.1016/S0009-2541(01)00357-6

971   Zack, T., & Luvizottow, G. (2006). Application of rutile thermometry to eclogites. *Mineralogy and*

972   *Petrology, 88*(1-2), 69-85.

973   Zack, T., Moraes, R., & Kronz, A. (2004). Temperature dependence of Zr in rutile: empirical

974   calibration of a rutile thermometer. *Contributions to Mineralogy and Petrology, 148*(4), 471-

975   488. doi:10.1007/s00410-004-0617-8

976   Zack, T., von Eynatten, H., & Kronz, A. (2004). Rutile geochemistry and its potential use in

977   quantitative provenance studies. *Sedimentary Geology, 171*(1-4), 37-58.

978   doi:10.1016/j.sedgeo.2004.05.009

979   Zhou, T., Li, Q., Klemd, R., Shi, Y., Tang, X., Li, C., & Liu, Y. (2020). Multi-system geochronology in

980   North Dabie eclogite: Ineffective garnet 'shielding'on rutile inclusions under multi-thermal

981   conditions. *Lithos*, 105573.

982

983

984
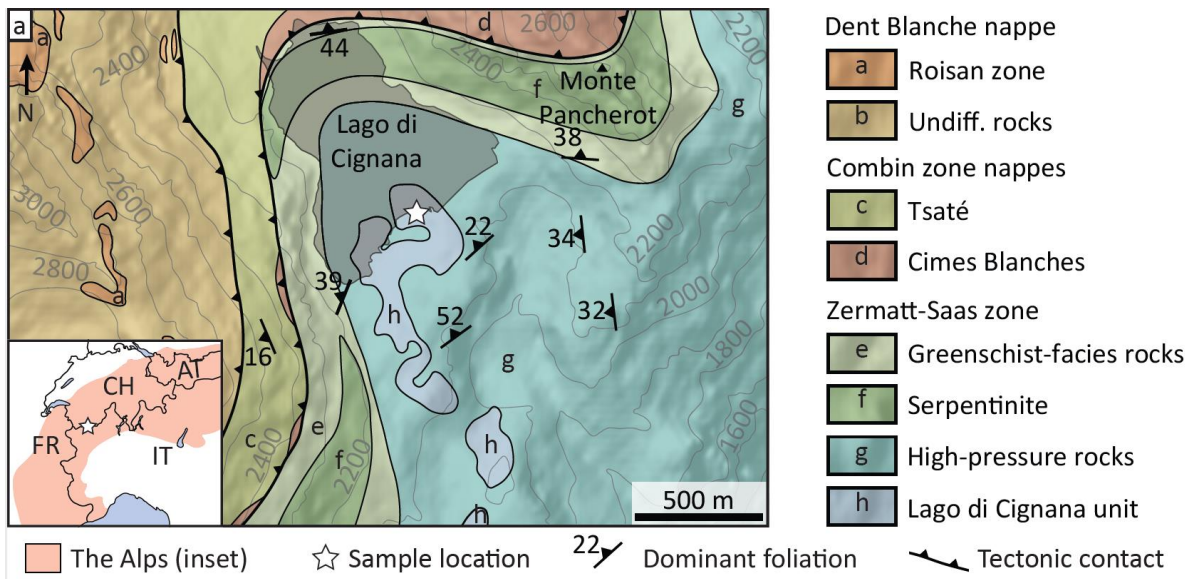
987 *Figure 1: a) Simplified geological map of the sample area around Lago di Cignana, modified after*

988 *Kirst & Leiss (2017) and references therein. FR = France, IT = Italy, AT = Austria and CH = Switzerland*
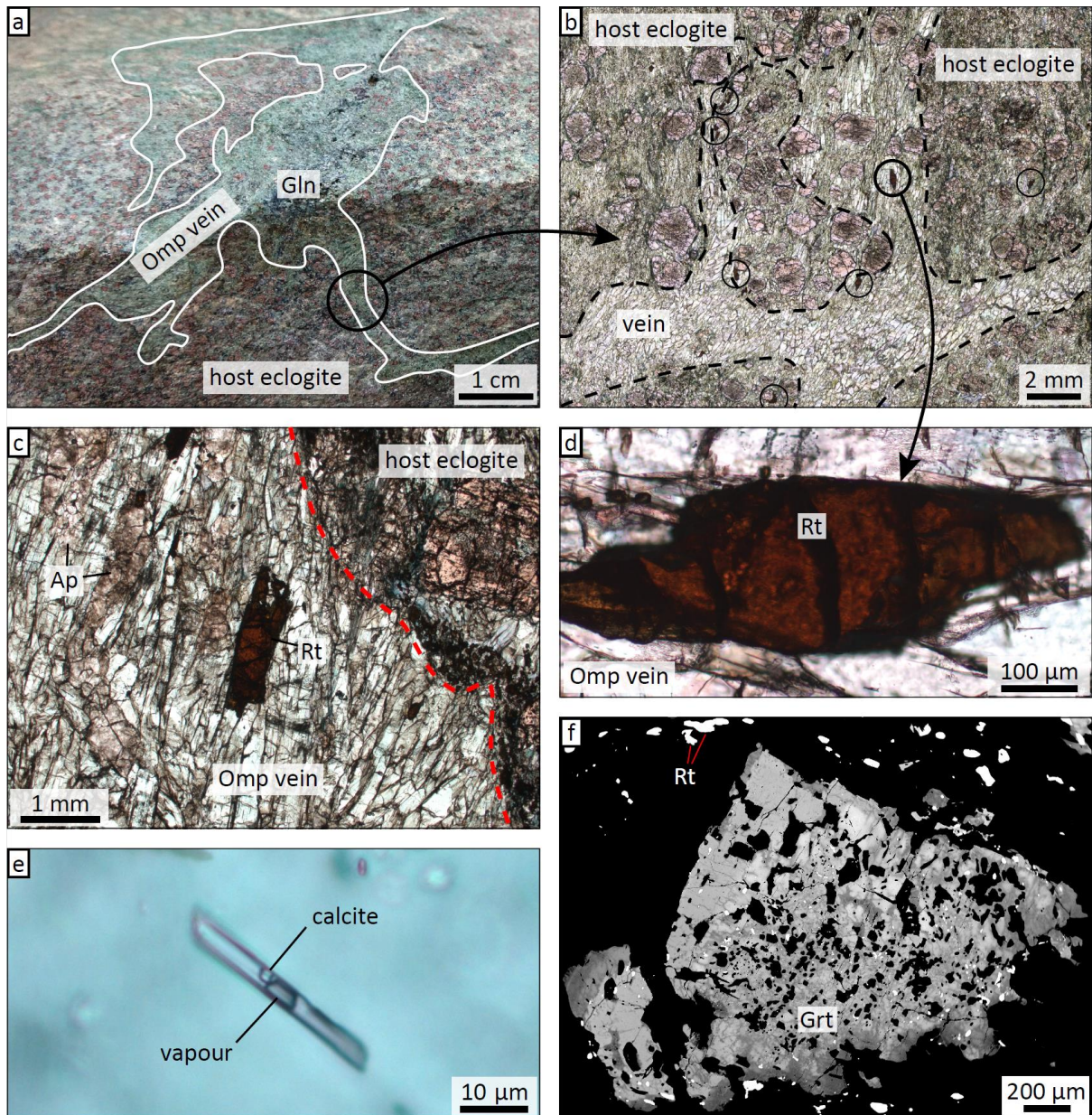
Figure 2: a) Outcrop photograph of eclogite containing an omphacite-glaucophane vein. b-e) Optical micrographs of analysed thick sections. b) Scan of a thick section that includes both omphacite vein and host eclogite. The boundary between the two is marked by the dashed black lines. Circles indicate the location of several large grains of rutile. The marked grain with the arrow leading to (d) is the grain selected at nanoscale analyses at Curtin University, Rt-1 (see Fig. 3). c) Closeup of a large rutile grain and the contact between the omphacite vein and the host eclogite, marked by the red dashed line. d) Close-up of the rutile grain selected for nanoscale analyses. e) A fluid inclusion in omphacite in the vein, containing a vapour bobble and a daughter crystal of calcite as identified with

Raman spectroscopy. f) BSE image of garnet in the host eclogite directly adjacent to the omphacite

999 *vein. Mineral abbreviations are from Whitney & Evans (2010).*
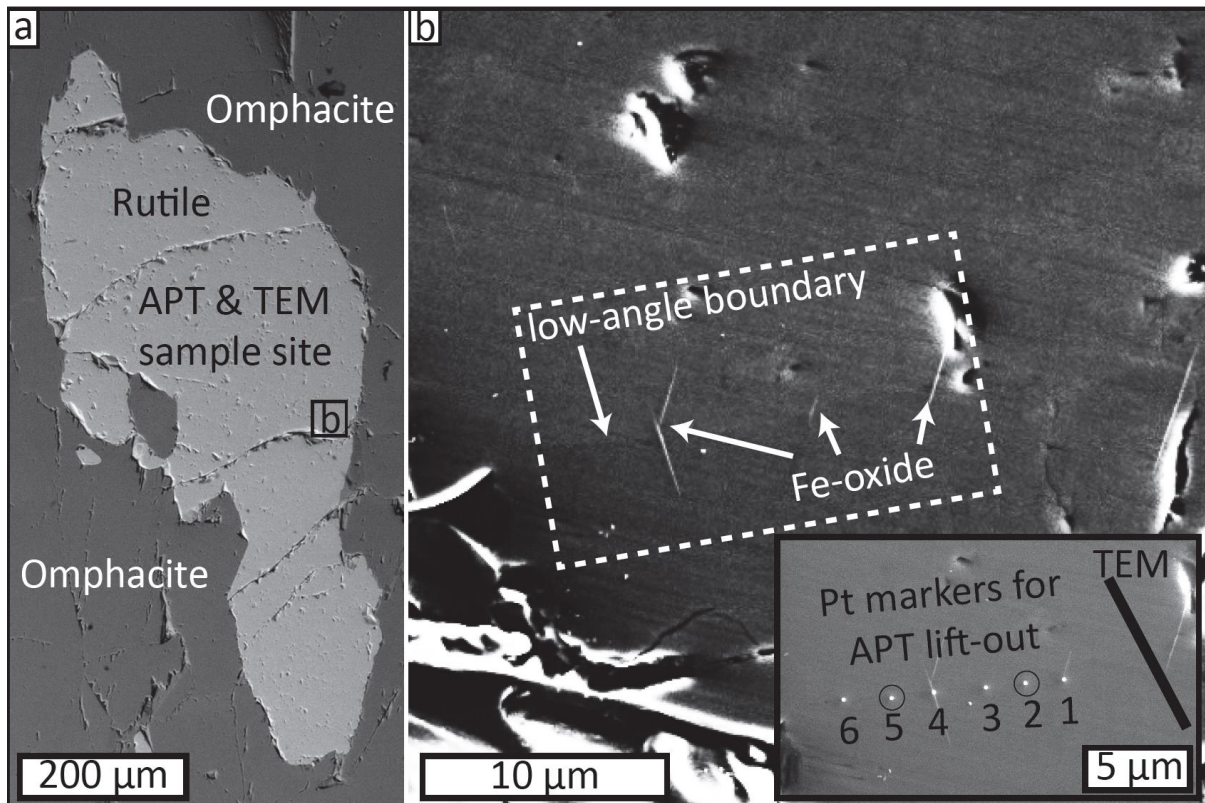
1000

1001 *Figure 3   : a) Backscatter Electron image of the rutile grain Rt-1 highlighting the APT and TEM lift-*

1002 *out area and demonstrating that the rutile grain is completely surrounded by omphacite. b) Close-up*

1003 *secondary electron image of the lift-out site. The low-angle boundary is made visible via the electron*

1004 *channeling effect. Fe-oxide exsolutions clearly intersect this boundary. The inset shows the deposited*

1005 *Pt-buttons that assist during preparation of the APT specimen. The encircled markers correspond*

1006 *with the two APT analyses that contain the LAB within the analytical volume. The TEM section was*

1007 *taken to the right-hand side of APT spec. 1.*
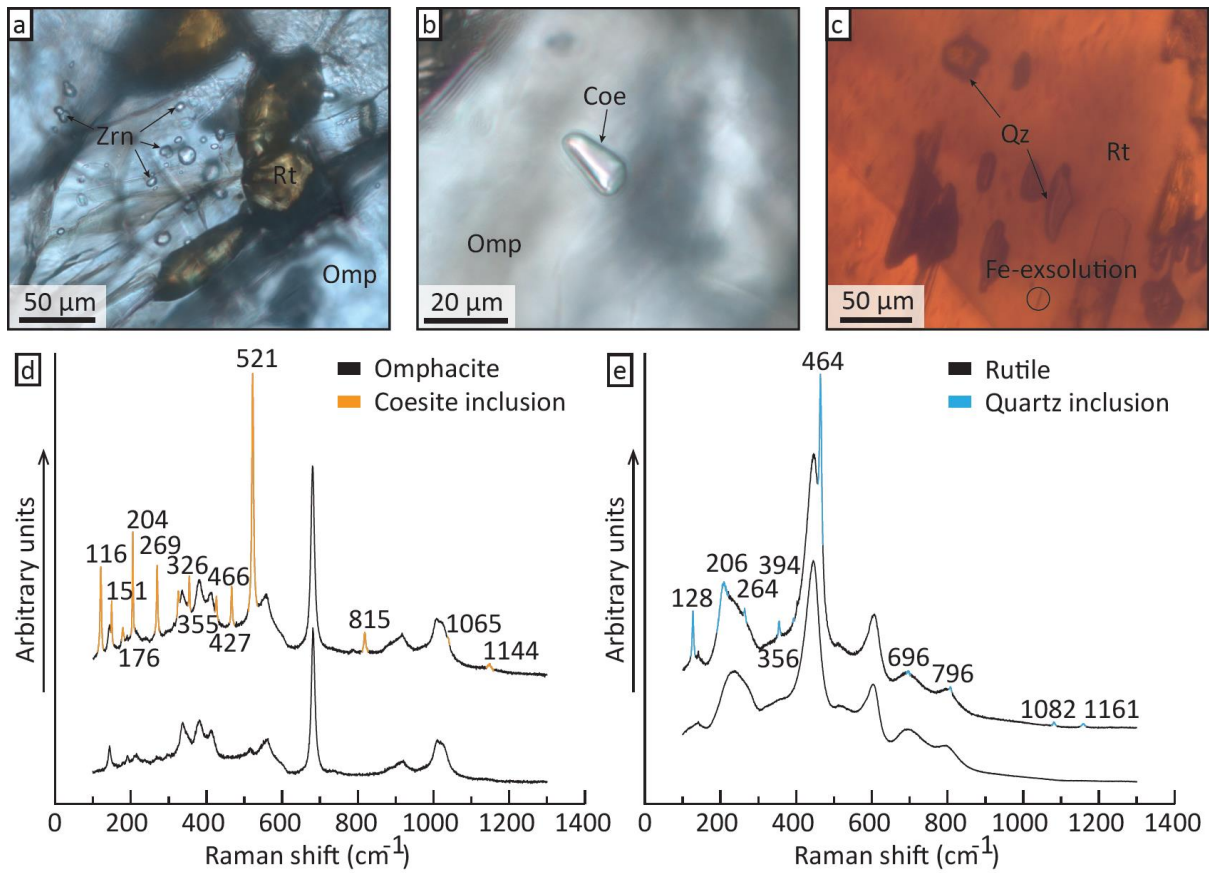
1008

1009 *Figure 4   : a–c) Micrographs taken with plane-polarized light revealing (a) the presence of zircon*

1010 *(Zrn) inclusion in omphacite (Omp), (b) a coesite (Coe) inclusion in omphacite, and (c) quartz (Qz) and*

1011 *Fe-rich inclusions in rutile (rt). Scale bars indicate 50 µm. d–e) Representative Raman spectra*

1012 *demonstrating the presence of a coesite inclusion in omphacite (d) and a quartz inclusion in rutile (e).*
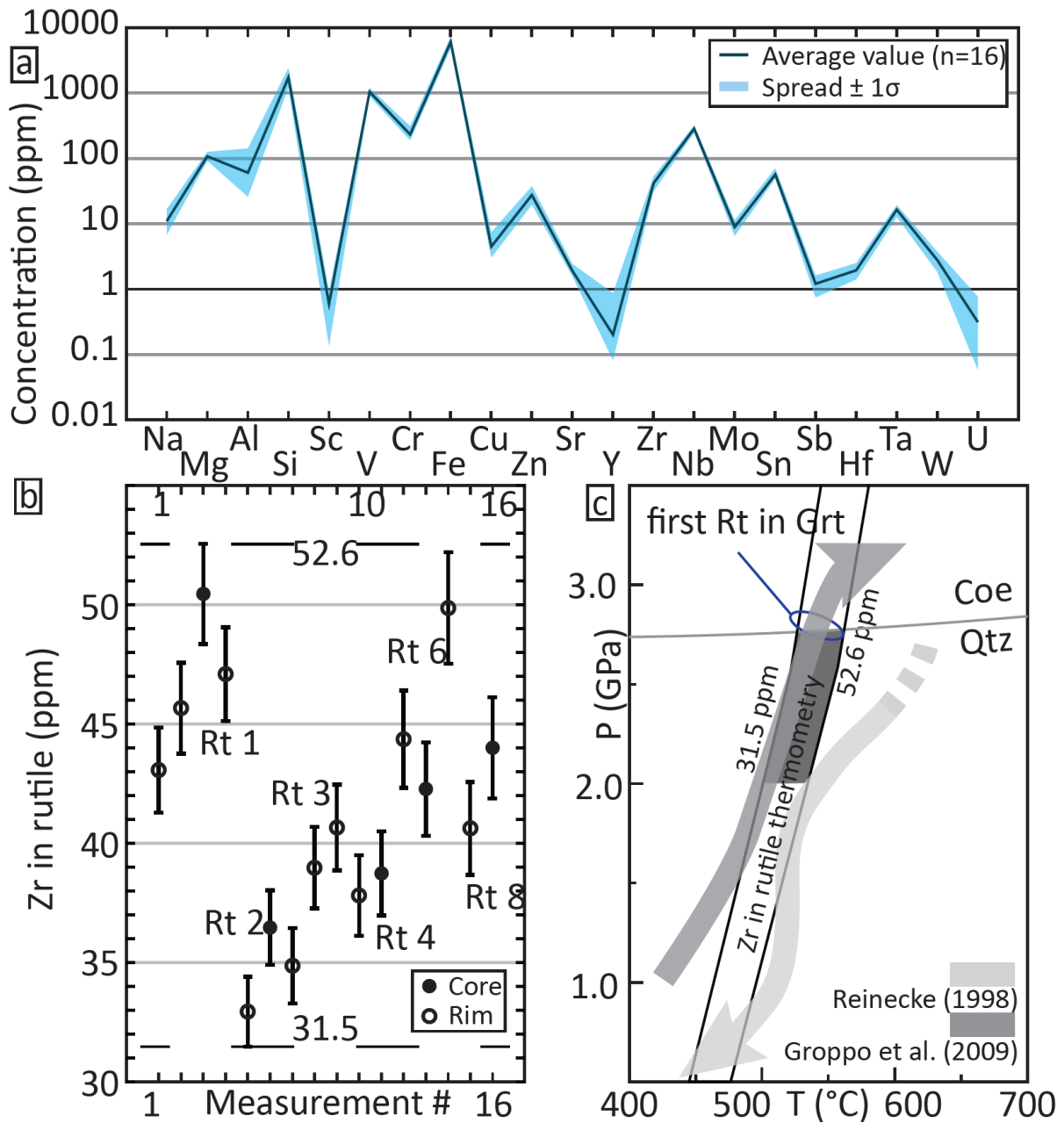
1013

Figure 5   : a) Elemental concentrations measured by LA-ICP-MS, with the average shown as a solid

1014

line. b) All measured concentrations of Zr in rutile, with error bars representing 2σ. Dashed horizontal

1015

lines indicate the full possible range of Zr concentrations based on these analyses. c) P-T-t diagram

1016

illustrating the metamorphic history, including the Zr concentrations in rutile and the corresponding

1017

temperature values using Zr-in-rutile geothermometry. "First Rt in Grt" indicates the approximate

1018

first occurrence of Rt inclusions in garnet, marked in P-T *space according to Groppo et al. (2009).*

1019

1020
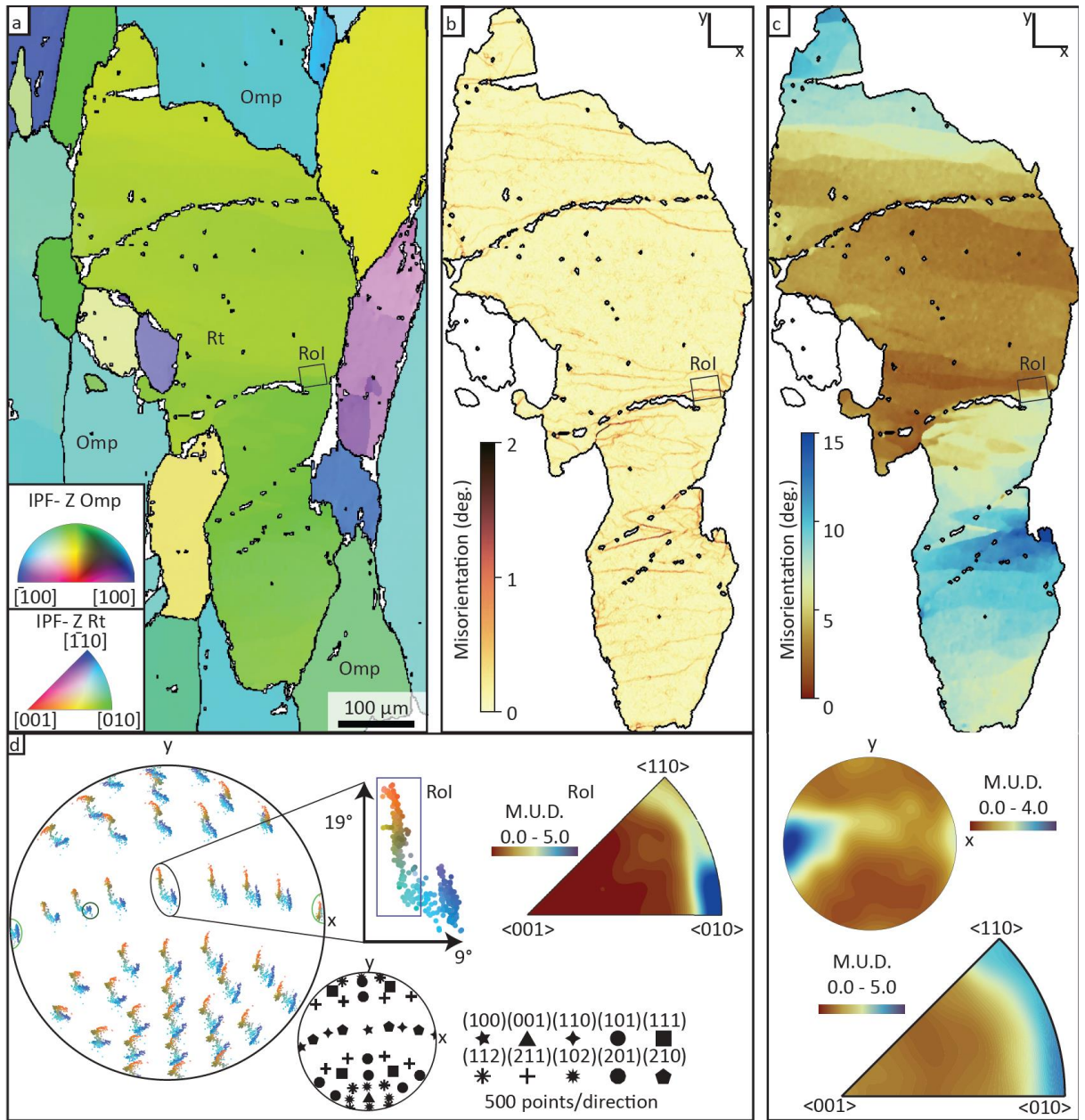
1021

1022 *Figure 6   : a–c) EBSD maps of the rutile grain of interest with the Z-axis of the map defined as*

1023 *normal to the page. The box marked RoI indicates the APT lift-out area. (a) Crystal orientation*

1024 *represented by the crystallographic direction aligned with the Z-axis of the map, (b) Local-*

1025 *misorientation map revealing the presence of low-angle boundaries. (c) Map of misorientation with*

1026 *respect to the mean orientation of the grain. The misorientation pole figure presents the*

1027 *misorientation axes of LABs in the specimen reference frame, whereas the misorientation inverse*

1028 *pole figure presents the same axes in the crystal reference frame. d) Pole figure with colours based*
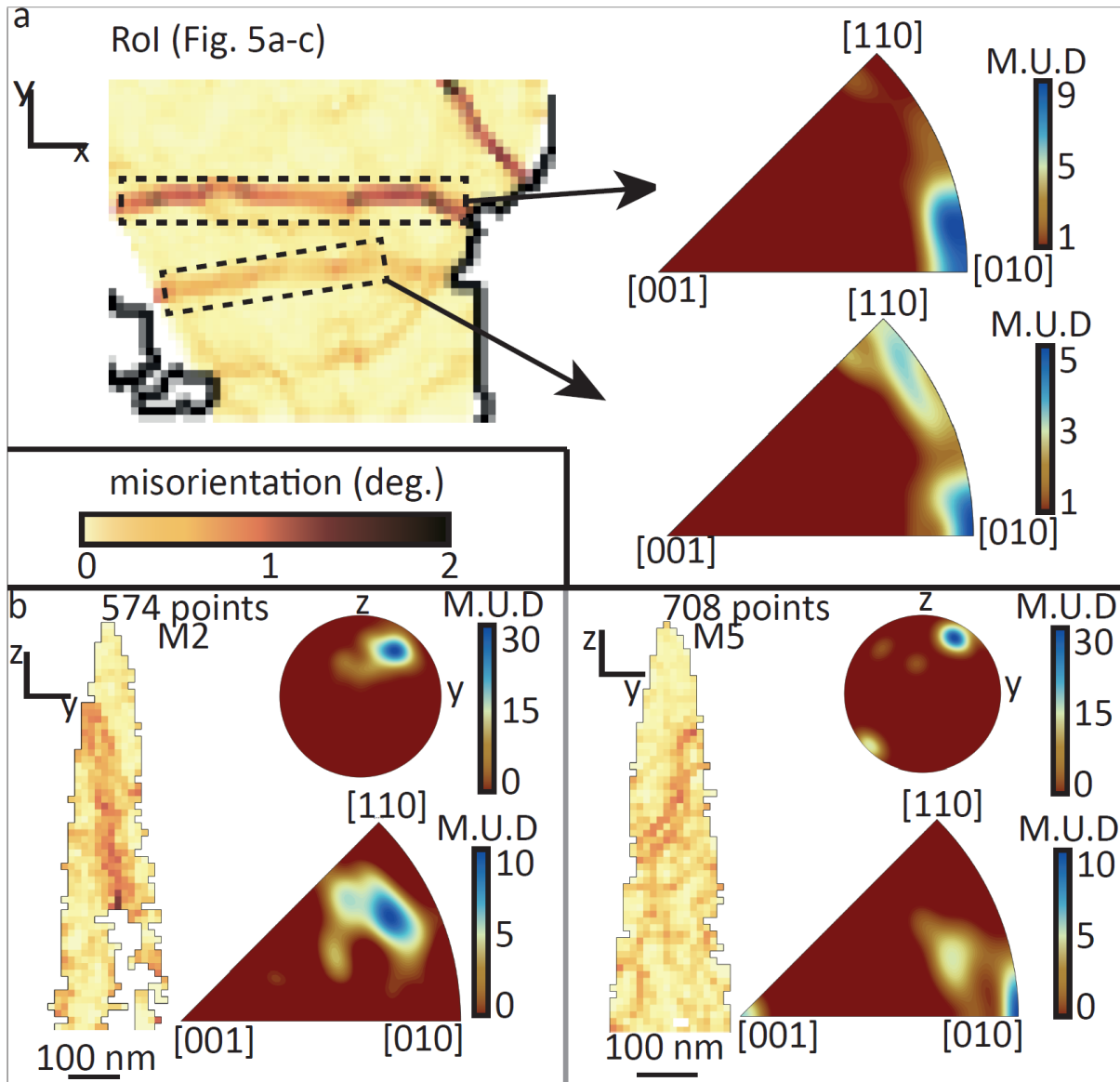
1033

1034   *Figure 7   : a) EBSD local-misorientation map of the RoI in Fig. 5. Misorientation inverse pole figures*

1035   *of two boundaries in the RoI are shown. b) TKD local-misorientation maps of, misorientation pole*

1036   *figures, and misorientation inverse pole figures of APT needles M2 and M5 extracted from the lower*

1037   *LAB in the RoI in (a). Respectively 574 and 708 have been plotted for M2 and M5.*
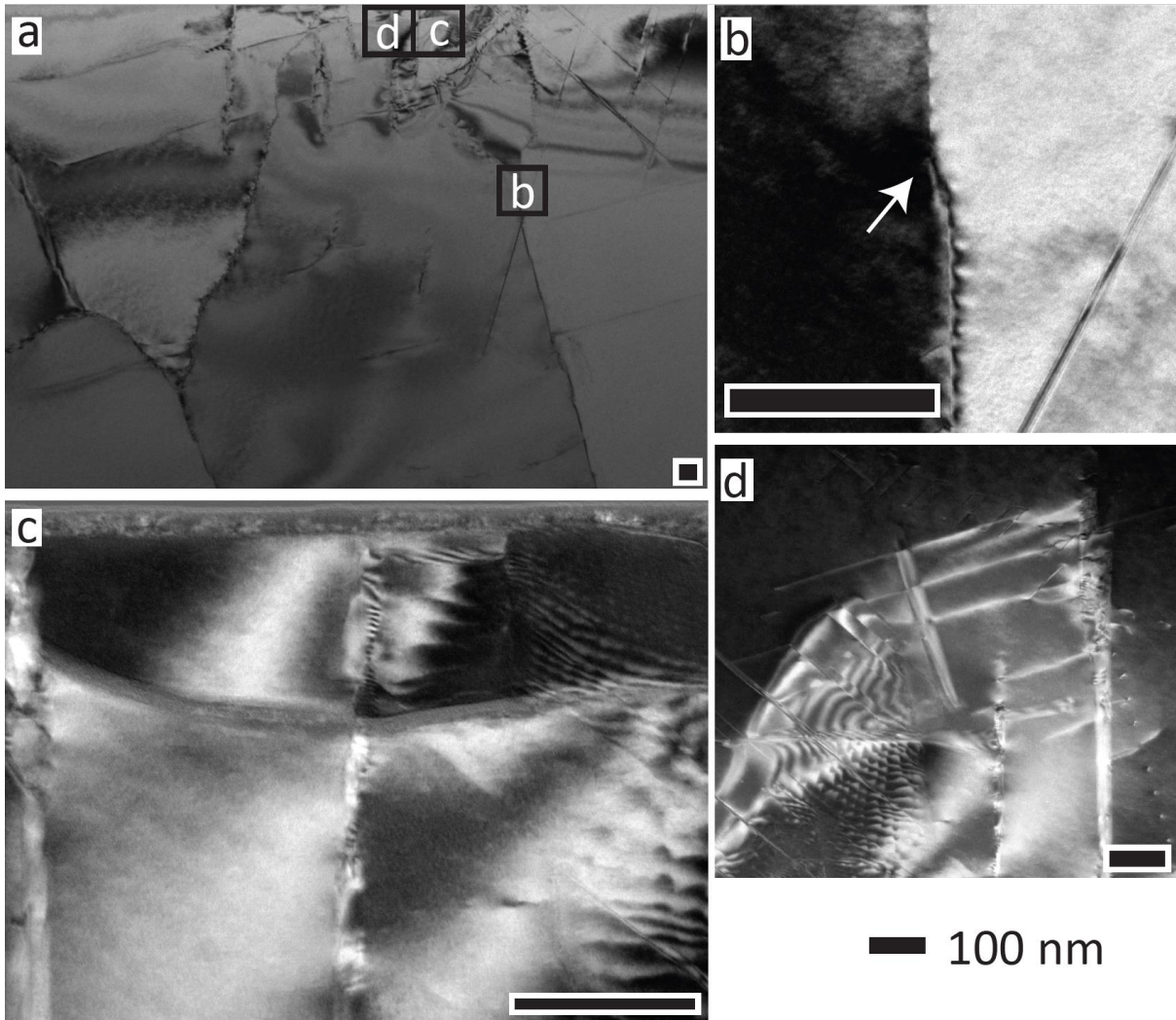
1038

Figure 8   : TEM images from the same ROI as the APT specimens. a) TEM HAADF image showing

the complexity of the microstructures present within deformed rutile. b) TEM HAADF and c-d) TEM

dark-field images showing the low-angle boundaries in greater detail. The white arrow in b) indicates

the offset of an otherwise continuous LAB. Note the slight changes in orientation of the LAB similar to

the change in the TKD maps in the APT needles.
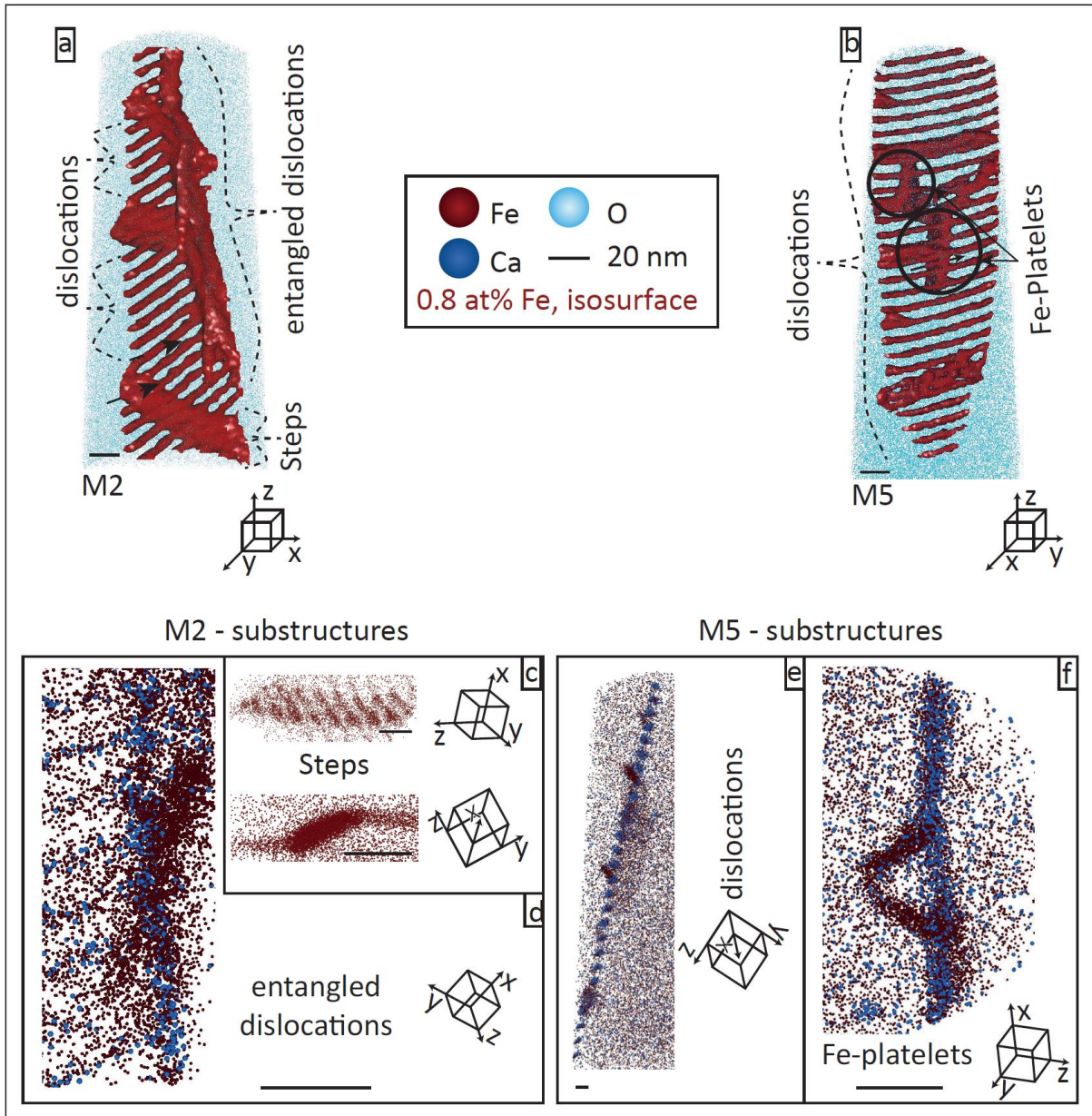
Figure 9 : 3D digital reconstruction of APT specimens 1 and 2. a–b) Isoconcentration surfaces of Fe

with several substructures labelled. c) Top and side view of the 'steps' showing the resulting offset of

approximately 10 nm. These 'steps' are also visible in (e) where they are free of any Ca enrichment. d)

Two entangled dislocations, of which one is in direct contact with the dislocations that form the LAB.

Note the difference in Ca distribution between the two dislocations (supplementary data DR-5). e)

View of the low-angle boundary along the dislocation cores showing the distribution of Fe and Ca. f)

View along the dip of the low-angle boundary in M5 showing the two Fe-platelets extending from

the LAB. The acute angles between the two platelets and the boundary are approximately 60°. The

black arrows in a and b refer the measurement location 1D concentration profiles (Fig. 10).
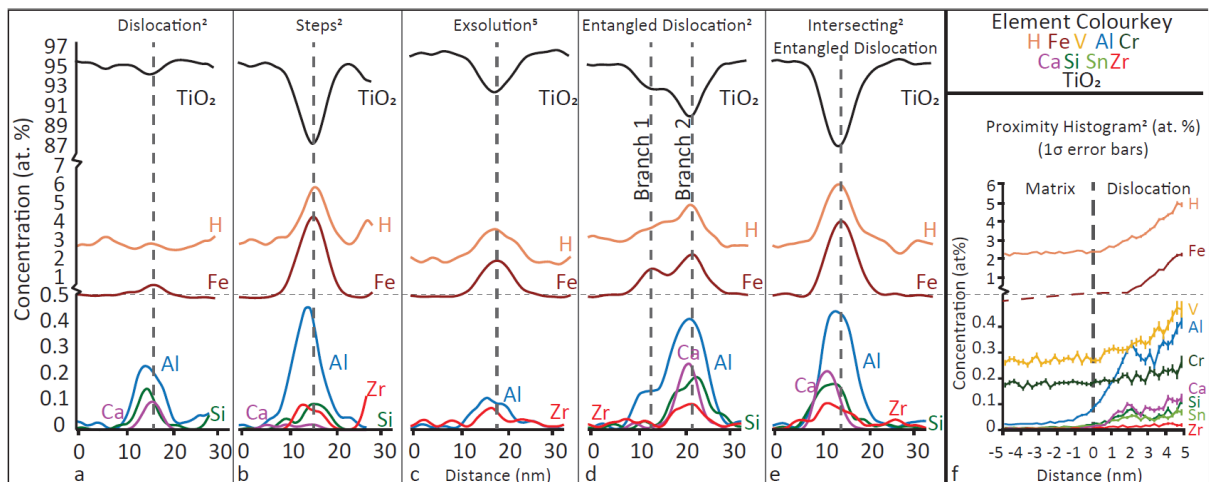
1055 *Figure 10   : Concentration profiles for the several substructures observed in the 3D APT*

1056 *reconstruction. The index number refers to the specimen number (M2 or M5). a–e) 1D concentration*

1057 *profile through single substructures observed in APT specimens 1 and 2. F) Proximity histogram for*

1058 *the full low-angle boundary. The location for the measurement is indicated in the reconstructions in*

1059 *Fig. 9 and the video in supplementary data DR-5.*
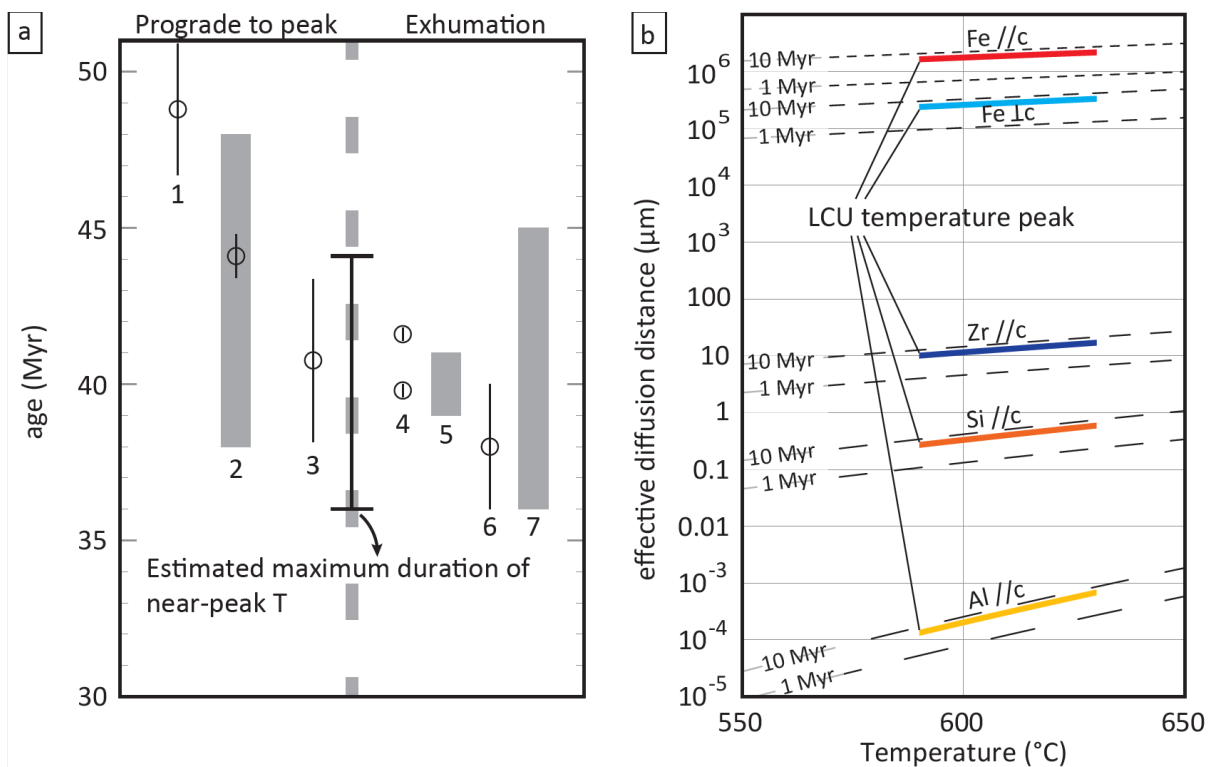
1061   *Figure 11   : a) Overview of geochronology literature for prograde-to-peak metamorphism of Lago*

1062   *di Cignana, and early exhumation for neighbouring units. Error bars are given as reported in*

1063   *literature, grey bars indicate a range of a whole dataset. Data sets and references: 1) Lapen et al.*

1064   *(2003), whole rock-garnet-clinopyroxene Lu-Hf; 2) Rubatto et al. (1998), zircon U/Pb; 3) Amato et al.*

1065   *(1999), whole rock-garnet Sm-Nd; 4) Skora et al. (2015), phengite-clinozoisite Rb-Sr; 5) Gouzu et al.*

1066   *(2016), white mica K-Ar; 6) Amato et al. (1999), whole rock-phengite Rb-Sr; 7) Reddy et al. (1999),*

1067   *phengite and miscellaneous other minerals Rb-Sr. b) Overview of effective diffusion distance for*

1068   *various relevant elements in rutile, as function of peak T of the LCU and the estimated duration*

1069   *thereof (5-8 Myr). Solid lines indicate effective diffusion distances in rutile of Fe, Zr, Al, and Si parallel*

1070   *to the c-axis, and Fe perpendicular to the c-axis   . Dashed lines indicate effective diffusion distances*

1071   *for fixed durations of peak temperature of 1 Myr and 10 Myr.*
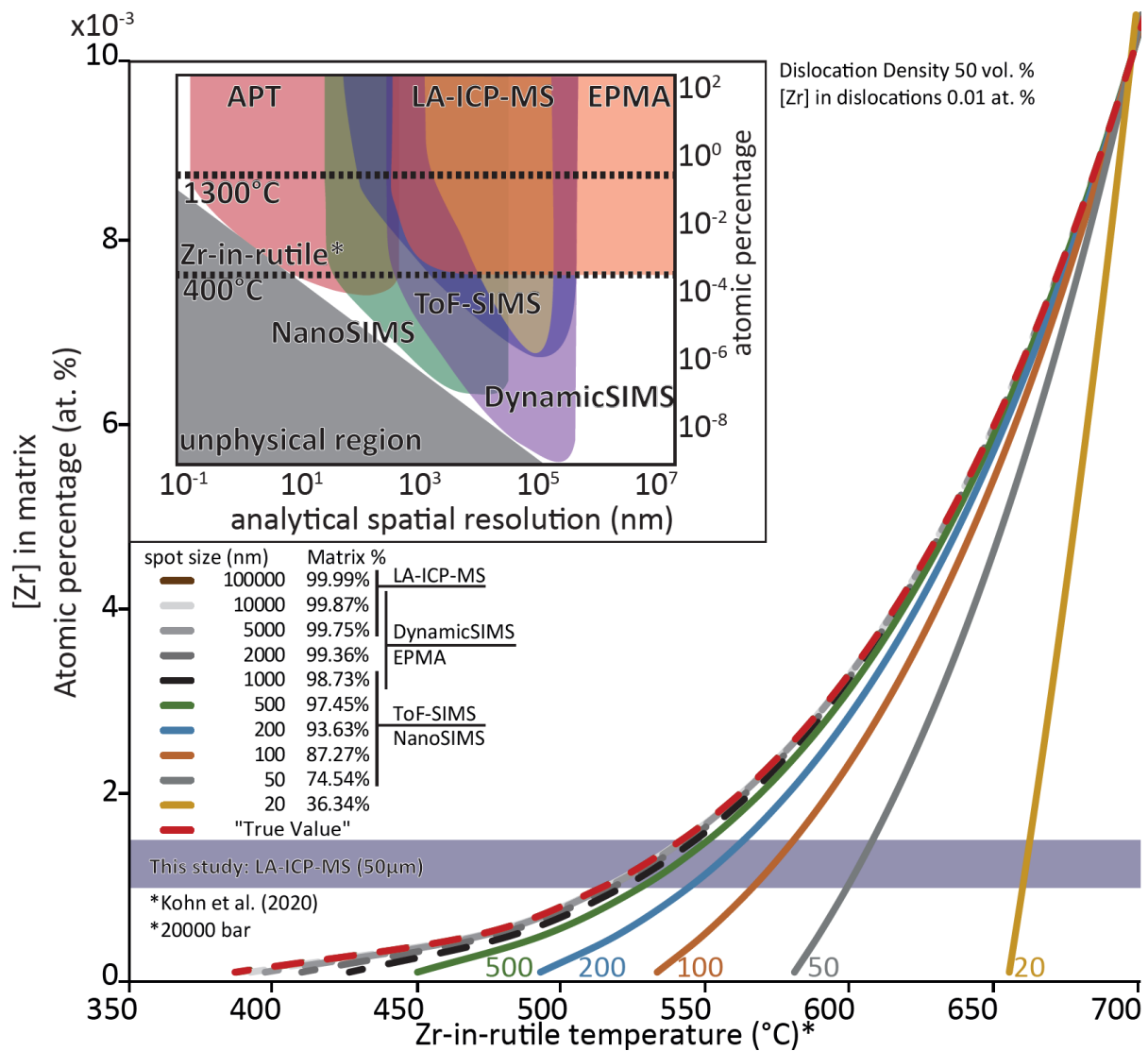
Figure 12: Temperatures obtained by Zr-in-rutile thermometry, and how these are affected by Zr-enriched LABs, as a function of Zr in the rutile matrix. Several spot sizes of the hypothetical chemical analysis are displayed along with the percentage of the sampled volume that consists of matrix. The inset is a diagram of the range of analytical resolution and detection limit for chemical analysis techniques used in geosciences. Element concentrations corresponding to two extreme temperatures for the application of Zr-in-rutile are given as context. APT = atom probe tomography, ToF = Time-of-Flight, SIMS = Secondary Ion Mass Spectrometry, LA-ICP-MS = laser ablation inductively coupled plasma mass spectrometry, EPMA = Electron Probe Micro Analysis